ENCAPSULATION AND DESIGN OF SCALABLE PACKAGING MATERIALS FOR THIN FILM PEROVSKITE SOLAR CELL APPLICATIONS

A Dissertation
Presented to
The Academic Faculty

by

Jinho Hah

In Partial Fulfillment
of the Requirements for the Degree
Master of Science in the
School of Materials Science and Engineering

Georgia Institute of Technology
May 2019

ENCAPSULATION AND DESIGN OF SCALABLE PACKAGING MATERIALS FOR THIN FILM PEROVSKITE SOLAR CELL APPLICATIONS

Approved by:

Dr. C. P. Wong, Advisor
School of Materials Science and Engineering
Georgia Institute of Technology

Dr. Meilin Liu
School of Materials Science and Engineering
Georgia Institute of Technology

Dr. Samuel Graham
School of Mechanical Engineering
Georgia Institute of Technology

Date Approved: April 19, 2019

To my beloved family

ACKNOWLEDGEMENTS

I would like to express a profound gratitude to my supervisor Prof. C. P. Wong for his guidance, encouragement, and endless support that he provided me during my Master's study. I would also like to extend my sincere gratitude to my thesis committee members Prof. Samuel Graham and Prof. Meilin Liu for providing their critical opinions and suggestions.

I would like to thank my current and previous group members including, Dr. Kyoung-Sik (Jack) Moon, Dr. Bo Song, Ms. Fan Wu, Mr. Jiaxiong Li, Mr. Chao Ren, and Mr. Minsoo Kang for their collaborations, suggestions, thoughtful discussions, and assistance. I would also like to thank my collaborators including Dr. Patxi Fernandez-Zelaia and Mr. Michael Sulkis for their fruitful discussions and endless help.

For my friends, I would like to thank Dr. Hyekyung Kim, Mr. Sangyun Han, Mr. Shinjae Kwon, Mr. Wootae Song, and Mr. Jaehyop Kim.

A significant amount of this work has been done in The Institute for Electronics and Nanotechnology (IEN), thus I would also like to extend my gratitude to the staff members for all the help.

Lastly, I would like to especially thank my parents and my brother for their support and love, without which this thesis and research would not have been possible.

TABLE OF CONTENTS

LIST OF TABLES

LIST OF FIGURES

LIST OF SYMBOLS AND ABBREVIATIONS

PSC	Perovskite Solar Cell
R2R	Roll-to-Roll
PV	Photovoltaic
PCE	Power Conversion Efficiency
FTIR	Fourier Transform Infrared Spectroscopy
XPS	X-ray Photoelectron Spectroscopy
FWHM	Full Width Half Maxima
SEM	Scanning Electron Microscope
TGA	Thermo-Gravimetric Analyzer
DSC	Differential Scanning Calorimeter

SUMMARY

There have been many attempts to improve the stability of the environmentally-sensitive perovskite solar cells (PSCs) from adverse environments. The next generation encapsulation method should be compatible with roll-to-roll (R2R) processing, which can manufacture thin-film PSC modules at large scale and make solar electricity economically competitive with conventional electricity generation. This work investigates the interface chemistry between the polymer backsheet and the polymer encapsulants to understand the moisture, thermal, and UV stability of the packaging materials for PSCs. First, surface modification on the commercially available PET backsheets was done using various types of silane-based coupling agents, and their adhesion profiles were studied upon damp-heat exposure on these samples. Second, thorough XPS analysis was conducted on the delaminated PET surface from the PET/EVA/PET encapsulation architecture upon the UV, thermal, and moisture aging to understand the degradation mechanism at the interface. Moreover, this work also includes encapsulant design by combining the polymer blends to improve the mechanical and chemical bulk properties of a PV encapsulant. In short, this work serves to investigate on the encapsulation methods to improve the reliability and lifetime of PSCs.

CHAPTER 1. INTRODUCTION AND BACKGROUND

Energy, a media for generating power, is derived from different types of sources. The world requires energy inevitably, and the demand for energy globally has increased rapidly in the past several decades due to the population growth, advancement in technology, and rapid industrialization and development, especially from the developing countries [1, 2]. Most of the energy requirements in world-wide are fulfilled by the conventional energy sources such as coal, gas, and oil, which are eventually expected to deplete in the future but, most importantly, are the main causes for the global warming. Scientists and policy makers have been in search for alternative source of energy that are environmentally satisfying and technologically conceivable [3]. Since the beginning of the 21st century, the transition into the renewable energy has been made. Among the renewable energy sources, there are hydroelectric, marine, wind, and solar energy sources, in which the latter is the most obvious and the most abundant terrestrial renewable energy source [2]. In addition, photovoltaics (PV) modules are currently the fastest growing technology; however, the service life of 25 years must be secured under field conditions for this PV technology to be economical [1]. Therefore, encapsulation of the PV modules is critical to their long-term reliability, which is directly related to their cost effectiveness.

1.1 Overview and Encapsulation

With fast-growing and arrival of innovative technologies and 3-D packaging modules, maintenance of their stability and improving their life-cycle are some of the challenges for engineers and material scientists. Encapsulation is one of the popular methods to ensure long term reliability and increase the production yield with the lowest

cost. Its purpose is to protect electronic, photonic, PV devices and modules, one of which being the solar cells, from an adverse environment such as high humidity, oxygen, hydrogen environment [4]. Because PV modules function in any type of outdoor environments, they can be susceptible to oxygen and moisture passivation that could lead to degradation, which then negatively affect the performance and lifetime of the device. Encapsulation of the packaging is not only the challenge, but also maintaining the solar cell's flexibility and transparency become an additional challenge to maximize the solar cell performance, quantitatively defined as power conversion efficiency (PCE). This narrow and strict limit of encapsulation of solar cells makes it even harder to choose the best combination of materials. This thesis and its related research provide concepts and methods to maximize the device stability through encapsulation and increase the overall life time of the solar cell, while maintaining its flexibility and transparency.

1.2 Encapsulation Requirements and Needs for Photovoltaic (PV) Modules

Manufacturing flexible, thin-film PV modules at large scale has the potential to make solar electricity economically competitive with conventional electricity generation [5]. PV module consists of frame, frontsheet, backsheet, encapsulant, solar cell (semiconductor), and junction box. **Figure 1.1** illustrates a typical architecture of a commercially available PV module. Within the PV module, the semi-conducting active cell absorbs photons from the sunlight and generates electron-hole pairs that flow through a circuit to generate direct current (DC) electricity. However, this active solar cell must be well-protected from any adverse conditions where the PV module is installed. Here, the latest encapsulation methods and its requirements for commercialized silicon solar cell and laboratory scale perovskite solar cells (PSCs) are discussed.

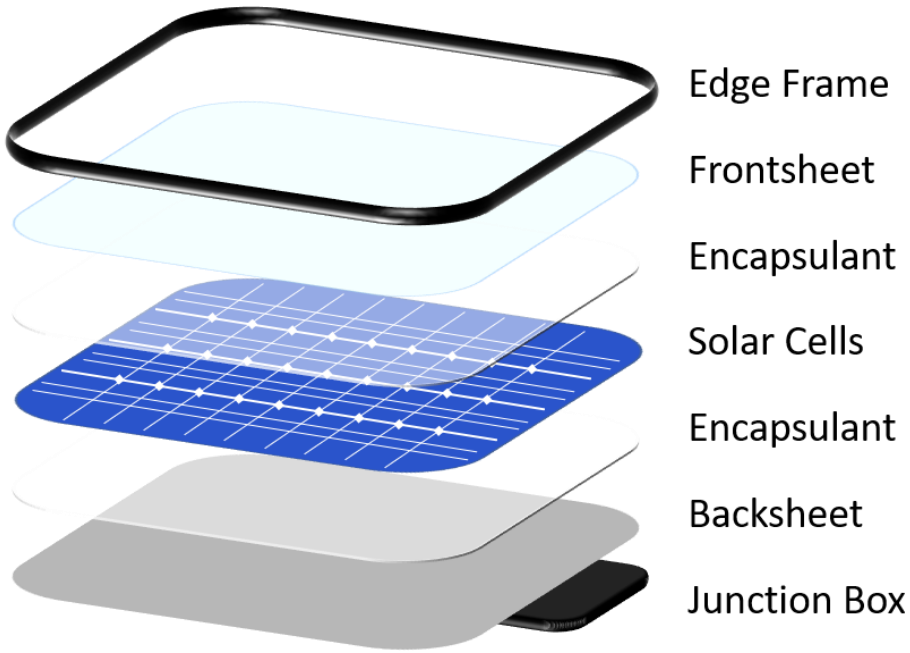

Figure 1.1 Layer-by-layer architecture of commercially available silicon PV module. Adapted from reference [6].

1.2.1 Silicon Solar Cells

In traditional silicon solar cells, their PV module packaging materials include glass as the frontsheet, aluminum frame, ethylene vinyl acetate (EVA) as an adhesive encapsulant material, and glass or flexible substrate as the backsheet, which are all required to ensure the reliability of solar PV modules. Note that EVA film has been the dominant encapsulant material in the PV industry since the 1985 [7]. Although the reliability of silicon solar cells is adequate, research has been on-going to improve EVA properties [8-10]. Commonly observed failures in silicon solar cells are module delamination and optical losses in encapsulant, in which EVA decolorizes from transparent to brown upon long-term exposure under the ultraviolet (UV) rays and its operating temperatures near 50 °C [7]. However, the current encapsulation technique utilized in silicon solar cells meets the

25-year life requirement, and due to the recently advanced PSCs, more research is conducted in improving the reliability of PSCs as these have not yet met the 25-year life requirement.

1.2.2 Perovskite Solar Cells

Perovskite Solar Cells (PSCs) have demonstrated outstanding performance, achieving PCE as high as 23.7% and theoretical efficiencies up to 31% [11, 12]. In addition, an even higher PCE can be obtained by combining the two silicon and PSC devices together, i.e. perovskite/silicon tandem solar cells [12]. Unlike the silicon solar cells, the instability of this organic-inorganic hybrid PSC device remains a significant hurdle to commercialization. Currently, PSCs only lasts up to 6 months at an outdoor environment, because PSCs are susceptible to harsh environmental conditions such as extreme amount of absorbed UV rays, temperature, and high humidity. Therefore, encapsulation of this PSC device is one of the top priorities to improve and maintain its stability [12-15]

Currently, glass-to-glass encapsulation method has been used and practiced at a laboratory-scale, where glass slides serve as both frontsheet and backsheet, and getter-filled poly(isobutylene) (PIB) and poly(dimethyl-siloxane) (PDMS) are used as the edge seal and encapsulant respectively [16]. This type of architecture, utilizing PIB as an edge seal, is required to protect the PSCs from adverse environmental conditions, especially from moisture. PIB is known for having one of the lowest water vapor transmission rates (WVTR) reportedly 0.01 to 0.001 $gm^{-2}\,day^{-1}$ [17], whereas PDMS elastomer, i.e. Sylgard 184, is ~900 $gm^{-2}\,day^{-1}$ [18]. It is also reported that a 1.25 cm wide getter-filled PIB edge

seal as a moisture barrier can pass IEC 61646 (1000 h at 85 °C/85% R.H.), which is equivalent to a 25-year lifetime at an outdoor environment [19].

However, for the next generation encapsulation method it would be valuable to minimize or eliminate the need for an opaque edge sealant. This will increase the available area for light-harvesting regions of PSCs and will simplify the encapsulation process, presumably aiding high-volume manufacturing as it removes an additional lamination step. It is also crucial that frontsheets and backsheets be replaced by transparent and flexible polymer barrier films for the next generation encapsulation method to be compatible with roll-to-roll processing. This would provide for fast, efficient, and large-scale processing of flexible thin film solar cells [20]. **Figure 1.2** compares the latest-generation encapsulation method of PSCs developed by McGehee group and their future-generation encapsulation architecture. Note that this figure is a simplified version, such that hole transport layer (HTL), electron transport layer (ETL), fluorine-doped tin oxide (FTO), indium tin oxide (ITO), and top and bottom metal electrodes are ignored.

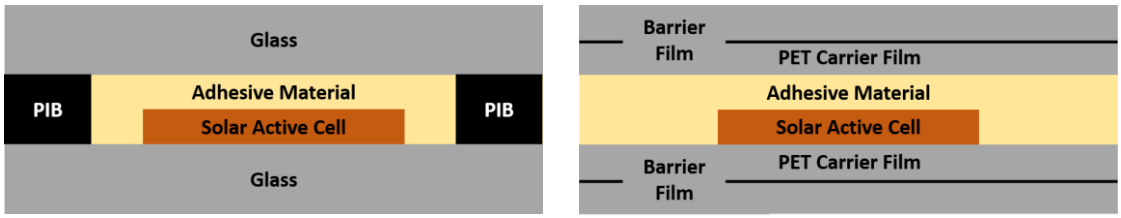

(a) (b)

Figure 1.2 Representative schematic design of PSC package (a) of 1st and 2nd generation encapsulation technique which utilizes opaque PIB and rigid glass substrates and (b) towards next generation encapsulation technique.

1.3 Materials for PV Module Packaging

1.3.1 Frontsheets and Backsheets

Frontsheets and backsheets are the most exposed parts among any other parts that make up the PV solar modules. They must have following features: optical transmission should be high (>89%) as the sunlight or phonons of specific wavelengths should be able to transmit through the cell and reach the active solar component to generate power, low WVTR, excellent UV stability. Note that flexibility of these frontsheets and backsheets are optional, and many PSCs have been fabricated on a rigid glass substrate with a titanium oxide layer processed at high temperature (>450 °C) [21]. However, manufacturing flexible, thin-film PV modules at low temperature, large scale, and even applicable for roll-to-roll system has been considered more appealing [20-22]. This high-throughput manufacturing technique compatible with roll-to-roll processing also makes solar electricity economically competitive with conventional electricity generation [5]. Among many, 3M is one of the renowned manufacturers for ultra-barrier solar films for organic photovoltaic (OPV) solar modules.

1.3.2 Encapsulants

The role of encapsulant resins are to bond and provide environmental and mechanical stability to multiple layers in PSCs against thermal and mechanical stresses [7, 16, 23, 24]. These resins should have high optical transmittance, good adhesion properties, and respectable mechanical properties to protect PSCs from such stresses [7]. More detailed summary of the most important bulk properties of an encapsulant is described in **Figure 1.3** [25].

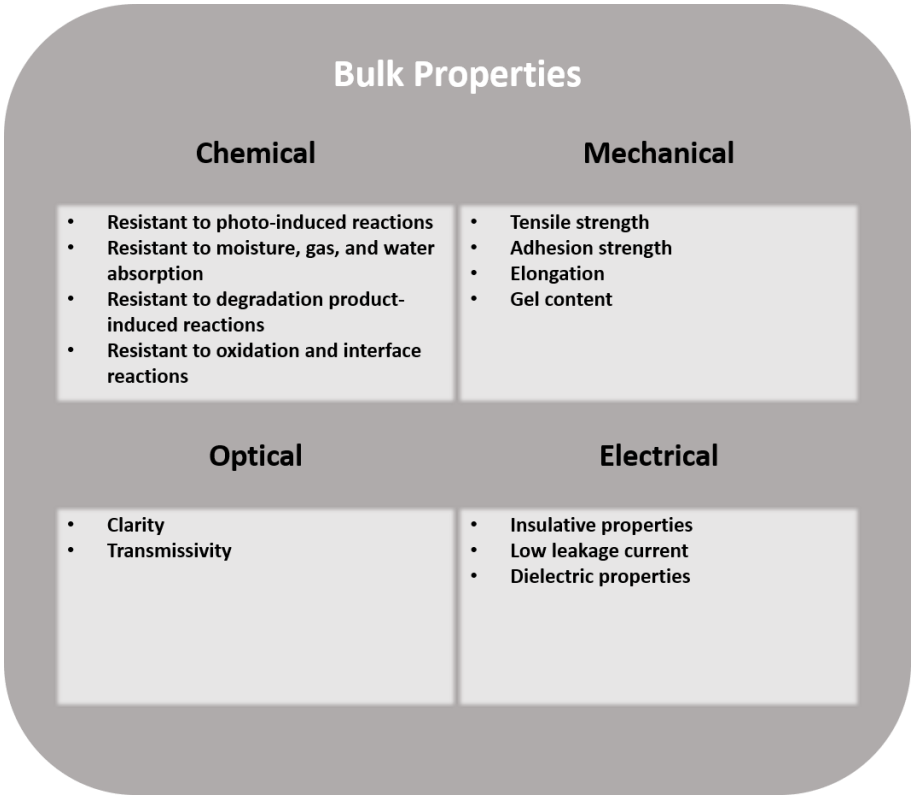

Figure 1.3 The most important bulk properties of an encapsulant. Adapted from reference [25].

In addition, most widely known and used encapsulant resins are listed in **Figure 1.4** with their chemical structures [7, 26]. Moreover, selected encapsulant resins used in recent studies [16, 24] are compared in **Table 1.1**. Note that thermoplastic polyurethane (TPU) contains hydrolytically unstable bonds in its backbone structure, which could lead to depolymerization making TPUs susceptible to creep and delamination. Also, TPU, thermoplastic polyolefin (TPO), and polyvinyl butyral (PVB) are thermoplastic materials. It is reported that thermoplastic materials, in contrast to thermosetting polymers such as PDMS and EVA, have creep and flow concerns at elevated temperatures [27]. The wide benefit of utilizing cross-linking agent containing thermosets (i.e. Pt-based catalyst for

crosslinking PDMS) is a better adhesion with the polymer and/or inorganic backsheets. The cross-linked chemical structure chemically bonds to the surface, whereas the thermosetting polymers rely on either ionic, hydrogen, or Vander der Waals forces (or in combination) for adhesion [26].

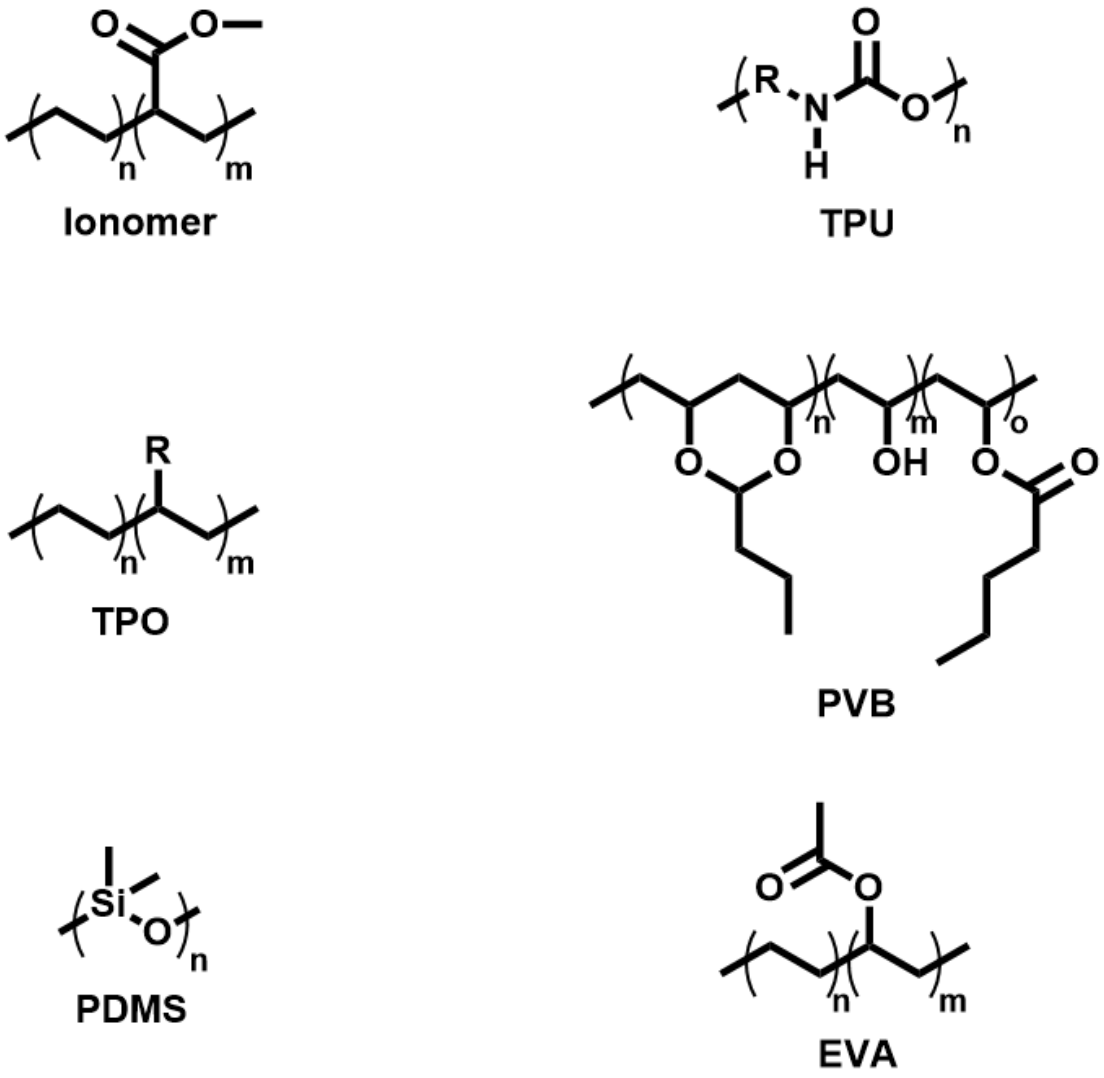

Figure 1.4 Chemical structures of widely accepted PV encapsulant resins.

Table 1.1 Comparison on the properties of the PV encapsulant resins.

Encapsulant Resin	Optically Transparent	UV Stable	WVTR ($gm^{-2}day^{-1}$)	Drawbacks
Ethylene Vinyl Acetate (EVA)	✓	✗	20–30 [24]	• Formation of acetic acid [28] • Potential for chemical corrosion and potential-induced degradation [29]
Polydimethyl Siloxane (PDMS)	✓	✓	~900 [18]	• Poor moisture barrier property [18]
Ionomer Polyolefin	✓	✓	0.66 [24]	• High elastic modulus [24] • Mechanically unstable [24]

In summary, EVA and PDMS are still widely used encapsulant materials for the PSC encapsulation applications; however, edge sealants are still in practice due to overcome the moisture stability issues, in which moisture ingress is a crucial failure mode associated with these PV modules [30].

1.3.3 Edge Sealants

Edge seals are required in PV modules, especially for the moisture-sensitive PSCs as the encapsulant materials cannot fully protect the device by their own due to a relatively high WVTR. Currently, PIB is widely used as an edge seal material as it can block moisture from entering the device due to its lowest WVTR among any other types of edge seals or encapsulants [17, 19]. An alternative edge seal candidate material is UV-curable epoxy; however, several properties (**Table 1.2**) show that PIB is much more cost-effective, has wider application temperature range, and has 3 to 4 magnitude difference in the WVTR. In addition, Li et. al. [17] reported a 50% drop in PCE of PSCs encapsulated with UV-curable epoxy just only after 6 days at room conditions and found that PIB is rather a promising packaging material for PSCs.

Table 1.2. Comparison on the properties of the edge seals for PV modules. Adapted from reference [17].

Edge Seal	WVTR ($gm^{-2}day^{-1}$)	Application Temperature (°C)	Material Cost (US $)
Polyisobutylene (PIB)	0.01–0.001	25–160	0.22
UV-cured Epoxy	16	25	145

In short, PIB is a leading-edge seal material for encapsulating PSCs; however, this getter-filled PIB is optically not transparent and contains plethora of fillers to have optimal UV-blocking, moisture-blocking, thermal, and mechanical properties. Latter section describes typical additives used in formulating encapsulant and edge seal materials for PSC encapsulation applications.

1.3.4 Filler Materials (Additives)

Different types of filler materials are added as additives for both encapsulants and edge seals specifically designed for PV module applications. Previously mentioned EVA encapsulant for PV module application contains 27-33 wt.% of vinyl acetate [26] with additives such as UV absorber, UV stabilizer, anti-oxidant, and curing agent to make the compound cross-linked thermoset [8, 25]. Note that adhesion promoter is also added for better adhesion with the inorganic or organic substrate material (i.e. backsheet). Because pure EVA copolymer is not resistant to UV radiation, both UV absorber and UV stabilizer are added as additives for this encapsulant material. **Table 1.3** lists commonly used chemicals used for EVA formulation.

Table 1.3 Formulation of EVA encapsulant. Adapted from reference [8, 25].

Component	Chemical Name	Chemical Structure	Weight Percent (%)
EVA Encapsulant	Ethylene Vinyl Acetate (EVA)	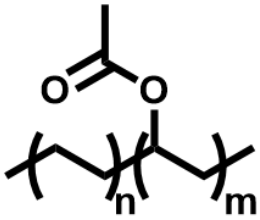	96.00–98.00
UV Absorber	Benzotriazole	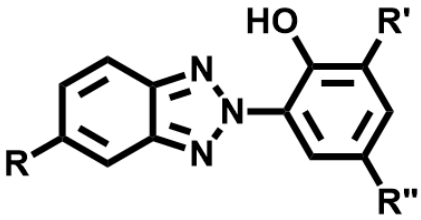	0.20–0.35
UV Stabilizer	Hindered Amine Light Stabilizer (HALS)	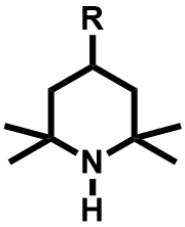	0.10–0.20
Anti-Oxidant	Phenolic Phosphite	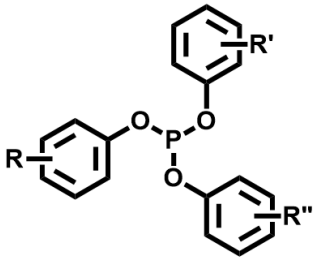	0.00–0.20
Curing Agent	Peroxide	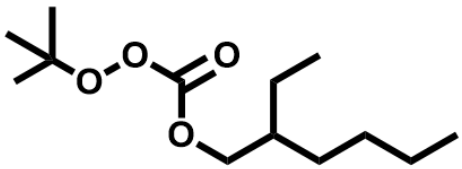	1.00–2.00
Adhesion Promoter	Trialkoxy Silane	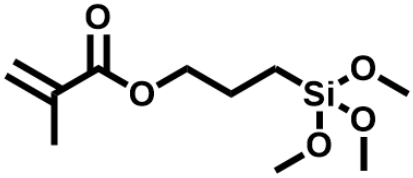	0.20–1.00

For edge sealants, different types of additives are added into a PIB polymer matrix. According to Kempe et. al. [19], molecular sieves (i.e. zeolites) are added as a desiccant and carbon black fillers are added as a UV blocker. However, it is possible that even PIB for PV encapsulation applications would have adhesion promoters within its formulation, although manufacturers do not fully disclose the exact formulation.

1.4 Research Objectives and Organization of the Dissertation

Previous sections provide versatile information respective to the need and the materials used for the encapsulation of the environmentally-sensitive PSCs. There have been many attempts to improve the stability of the PSCs from adverse environments; however, few of the successful ones have employed rigid glass as a substrate as frontsheets and backsheets.

In this research, instead of the rigid glass, flexible polymer barrier film and commercially available Polyethylene terephthalate (PET) are used as frontsheets and backsheets. Also it is important to understand the interface chemistry as moisture penetrates through the interfacial regions between the adhesive materials (encapsulants and edge seals) and frontsheets and backsheets. Not only moisture behavior is studied, but also thermal and UV radiation induced failures at the interface are analyzed. In short, interface engineering is of top priority investigated in this dissertation. This research, therefore, aims to investigate in such field that would improve the reliability and lifetime of PSCs. Furthermore, several commercially available encapsulants and edge seals are characterized to observe their moisture stability of the calcium surrogate sample, designed to improvise for real PSC modules. Also, their adhesion behavior was also characterized.

According to the objectives described above, this dissertation is organized their details are outlined as following:

- Chapter 2 will investigate the thermal and moisture stability of PDMS-based adhesive bonded to the surface-modified polymer backsheets using coupling agents and physical treatments for PSC module packaging applications. Surface modification on the PET backsheet was done chemically by organic silane-based coupling agents and physically by UV/Ozone treatment.
- Chapter 3 will investigate the UV, thermal, and moisture stability of EVA adhesive bonded to the PET backsheet. This chapter will address the interface chemistry of the delaminated samples upon individual aging condition.

Finally, Chapter 4 will summarize the achievements and contributions of this dissertation followed by addressing the future work that would strengthen the research in this field and for other encapsulation applications.

CHAPTER 2. INTERFACE ENGINEERING ON THE BACKSHEETS OF PV MODULES USING UV/OZONE AND SILANE-BASED COUPLING AGENTS

2.1 Introduction

Manufacturing flexible, thin-film photovoltaics at large scale has the potential to make solar electricity economically competitive with conventional electricity generation [5]. Furthermore, PSCs, which use organic-inorganic hybrid materials, have swiftly gained interest from many researchers and engineers in the PV community due to their promising properties and high energy conversion efficiencies (i.e. PCE) as high as 23.7% and theoretical efficiencies up to 31% [11, 12]. However, with this introduction to new thin film technologies, maintaining the reliability becomes more difficult as the overall thickness of the components are getting thinner to maintain flexibility. In addition, one of the main weaknesses of PSCs and other thin-film technologies is that they are particularly sensitive to water vapor and oxygen, which leads to degradation and negatively impacts the performance and lifetime of the devices [13-15]. Therefore, encapsulation materials must be used to protect these moisture sensitive devices from the adverse environment [4, 24]. Packaging materials, including adhesives, encapsulants, protective frontsheets and backsheets, are essential for manufacturing reliable PV modules [7].

Typically, an edge sealant is utilized to maximize the moisture stability of environmentally-sensitive PSCs. However, utilizing an edge sealant is considered a challenging method, and removing the need to edge-seal the solar cell can reduce the

manufacturing cost. Thus, for future generation encapsulation technique, developing materials that can both serve as an edge seal and adhesive material would be ideal for processability for large scale PSC manufacturing. However, when removing the moisture blocking PIB-based edge seal material, moisture stability of a package would be a huge concern. Therefore, possible solution to this problem is to reduce the free space at the interfacial regions to exclude water molecules from penetrating and accumulating at the interfacial regions [31]. These can be achieved by surface or interface engineering on the substrate materials to enhance the interfacial adhesion strength between the substrate and the adhesive material. In this work, the area of interest is the interface between the barrier film (backsheet) and the encapsulant material. We have isolated this interface by creating a symmetrical structure illustrated in **Figure 2.1**. The PET substrate is employed as a carrier layer for multilayered barrier films, and the adhesive material is adhered to the top and bottom of the PET surfaces (**Figure 2.1**).

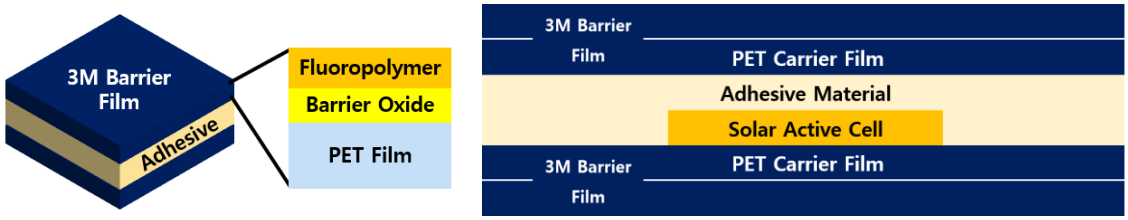

Figure 2.1 Schematic representative design of PSC package. Adhesive layer is sandwiched between the two 3M Barrier Films, which are structured in three-layers.

So far, there have been many efforts to improve adhesion strength between polymers and substrates. Gotoh and co-workers studied surface modification of PET substrates using UV excimer light and atmospheric pressure plasma (APP) jet to induce hydroxyl and carboxyl functional groups that reduces both advancing and receding contact angles to

increase wettability of polymer substrates [32]. Jorgenson and co-workers studied methods to improve adhesion strength using plasma etching and reported the adhesion strength degradation profile under damp-heat environment of ethynyl vinyl acetate (EVA)/glass interface [33]. Walzak and co-workers studied effect of UV, Ozone, or both treatment of polypropylene and PET and reported that combination of both treatment in together yielded 50° after 10 minutes of treatment for advancing angle and 0° within 3 minutes of treatment, which were the lowest values among different treatments of their study [34]. However, there has not been a full report and understanding of chemically surface-treated PET, especially on the adhesion strength behavioral change between the modified PET and the barrier adhesive upon thermal and moisture aging of the designed package for PSC module applications. Although the barrier film may primarily block incoming moisture, the moisture ingress through the interfaces between adhesive and carrier film surfaces could be detrimental to the active cells. Thus, strong adhesion at such interfaces is required for high reliability. Due to this nature, surface treatment on the barrier film serves to improve the interfacial adhesion strength and prolong the moisture and thermal stability.

The proposed solution-deposited adhesive in this study is a commercially available PDMS-based thermally cured adhesive designed for PV applications, which can be processed in a continuous feed system. Furthermore, we utilize surface modification of the PET substrate surface by UV/Ozone treatment, spray-coating the silane-based coupling agents, and both in combination prior to applying the adhesive layer. This work reports here an enhanced interfacial adhesion strength of a silicone adhesive via different types of surface treatments on a barrier film, without aging, after moisture aging in the environmental chamber (60 °C/90% R.H.), and thermal aging in the furnace (60 °C/Dry).

Additionally, we assume that none of the treatments described in this work impact the optical properties of the PDMS or the barrier film based on qualitative observations. To characterize the changes under different environmental conditions, several studies were employed such as T-peel tests and surface functional groups characterization via contact angle study and Fourier-Transform Infrared (FTIR) analyses. All samples were compared with an untreated control sample. This work serves to report our progress in improving PV packaging design to create highly stable thin film PV modules that could are also be compatible with roll-to-roll processing.

2.2 Experimental

2.2.1 Materials

A transparent, two part-addition cure PDMS adhesive (QSil 216) was purchased from Quantum Silicones, and a multilayer barrier film (204.5 μm in thickness) with a PET carrier was provided by 3M. Coupling agents, (3-Aminopropyl) trimethoxysilane, 98% (APTES) and (3-Glycidoxypropyl) trimethoxysilane, 97% (GPTES) used to treat the PET films were purchased from Alfa Aesar and (vinyl) trimethoxysilane (VTMS) purchased from Silqest.

2.2.2 UV/Ozone Physical Treatment and Silane-based Coupling Agents Chemical Treatment and Sample Fabrication

In this study, to enhance the interfacial adhesion strength between PDMS and barrier film, we employed chemical surface treatments including functionalized silanes and physical surface treatment using 30 minutes of UV/Ozone treatment. More specifically five

different surface treatments on the PET side of the barrier film are (A) APTES, (B) GPTES, (C) VTMS, (D) UV/Ozone, and (E) UV/Ozone & VTMS. Please note these sample designations, which will be used to label the sample type throughout this paper. illustrates functionalized-silanes used in this experiment.

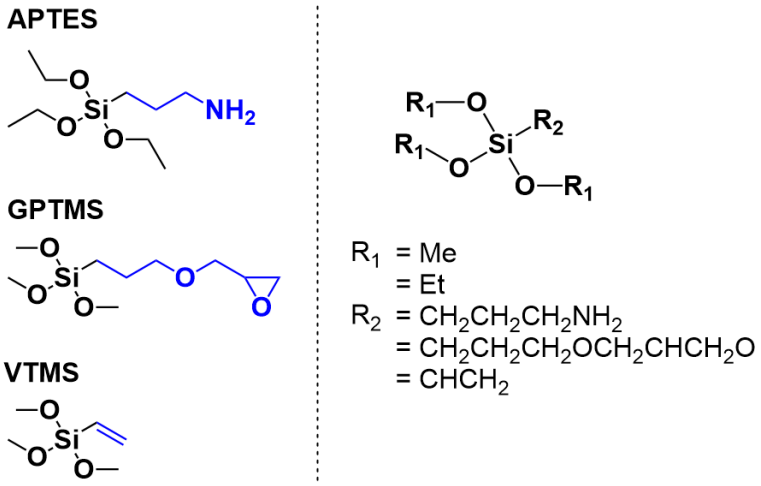

Figure 2.2 Schematic of chemical structure of coupling agents (functionalized-silanes) used for chemical surface treatments.

The barrier films for all samples were rinsed using acetone and isopropyl alcohol (IPA), respectively and were thoroughly dried with dry air. APTES, GPTES, or VTMS (100 mg) were mixed with an aqueous solution of 95% ethanol and 5% water (wt./wt.) to yield hydrolyzed chemical solutions necessary for surface treatment.

For the UV/ozone treatment, the barrier film was placed inside a UV/ozone chamber (Novascan, Boone, IA) with the PET surface facing-up. The sample was treated for 30 minutes at room temperature condition (25 °C). This condition was chosen to yield the highest surface energy of the PET surface from the previous study [35]. The surface treatment solution was spray-coated onto the PET-side of the barrier film and was dried at

ambient conditions until the ethanol and water evaporated. Note that samples treated with both UV/ozone and chemical surface treatment were done sequentially **Figure 2.3**.

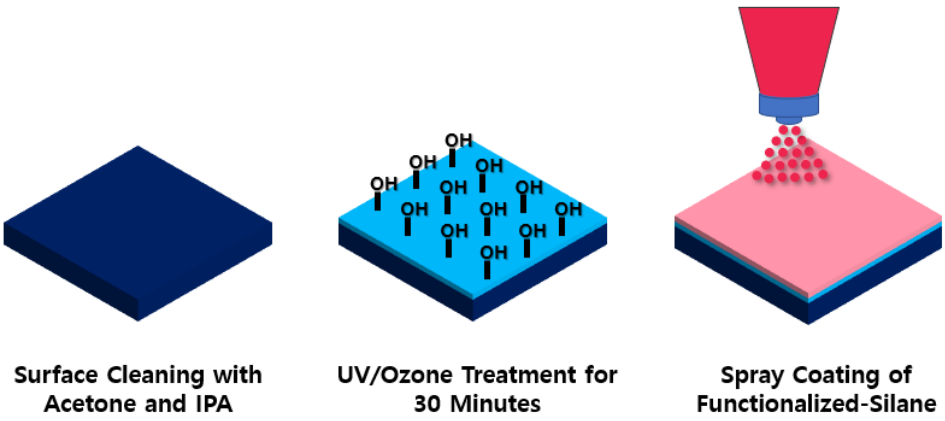

Figure 2.3 Schematic showing process flow of sample fabrication for UV/Ozone treatment followed by VTMS (Sample E) chemical spray coating of organic-silanes. Sample A to C is fabricated using the first and the last step only, whereas Sample D is fabricated using the first two steps.

Lastly, two-part PDMS was prepared according to the manufacturer's specifications. Once the surface was dried, PDMS mixture was coated on top of the PET with a roller. Coated PDMS adhesive was vacuumed at a pressure of 29 inches Hg inside the vacuum chamber for at least 5 minutes to remove any air bubbles, and a second barrier film was laminated onto the PDMS to create a symmetrical PET/Adhesive/PET stack (**Figure 2.1**). The assembly was then cured at 100 °C for 1 hour.

2.2.3 Contact Angle Measurement

Contact angles were measured for UV/Ozone treated barrier films with contact angle goniometer (ramé-hart, Succasunna, NJ) with DROP image Advanced software to

study the dependence of treatment time on surface energies. Surface energies were determined by calculating the dispersion (γ_s^d) and polar components (γ_s^p) using harmonic and geometric mean methods described below in equations (2.1) and (2.2), respectively [36-39].

$$\left(1+\cos\theta_i\right)\left(\gamma_i^d+\gamma_i^p\right)=2\left(\sqrt{\gamma_i^d\gamma_s^d}+\sqrt{\gamma_i^p\gamma_s^p}\right) \tag{2.1}$$

$$\left(1+\cos\theta_i\right)\left(\gamma_i^d+\gamma_i^p\right)=4\left(\frac{\gamma_i^d\gamma_s^d}{\gamma_i^d+\gamma_s^d}+\frac{\gamma_i^p\gamma_s^p}{\gamma_i^p+\gamma_s^p}\right) \tag{2.2}$$

Note that total surface energy (γ_s) of the substrate surface is equal to the arithmetic sum of the dispersion (γ_s^d) and polar components (γ_s^p) as shown in equation (2.3).

$$\gamma_s=\gamma_s^d+\gamma_s^p \tag{2.3}$$

Two probe liquids, deionized water and hexadecane ($H_{16}C_{34}$) were used for contact angle measurements [40]. These values were used to simultaneously solve individual equation for harmonic, equation (2.1), and geometric, equation (2.2), mean methods given appropriate data from the contact angle measurements, where γ_i is the surface tension or surface energy of the probe liquid and γ_s is surface energy of the substrate. All probe liquid droplets were approximately 5 µL in volume.

2.2.4 Thickness Measurement and T-Peel Tests

The thickness of each sample was measured in several locations using a caliper to verify that uniform layer of adhesive was deposited. A Universal Testing Machine (Test Resources, Shakopee, MN) was used to perform displacement-controlled T-peel experiments at 100 mm/minute. Maximum and mean peel-off forces were calculated using the software. All peel test samples were fabricated with 1 cm in width. A schematic of the

T-peel samples and test set-up is shown in **Figure 2.4**. Note that color-codes of the barrier films in **Figure 2.4a** are equivalent to that in **Figure 2.1**; therefore, the adhesive layer is sandwiched by sky-blue represented PET layer of the barrier film.

(a) (b)

Figure 2.4 Schematic representative of (a) T-Peel test sample and (b) T-Peel test setup.

2.2.5 Fourier Transform Infrared Spectroscopy (FTIR) Characterizations

FTIR spectra were taken using Thermo Scientific Nicolet iS5 FTIR spectrometer, installed with iD7 ATR accessory. FTIR samples were prepared as illustrated in **Figure 2.3**.

2.3 Contact Angle and Surface Energy Profiles upon Surface Treatments

A contact angle study was conducted to determine the change in surface energy with respect to UV/ozone exposure time on the barrier film. An increase in surface energy indicates the formation of functional groups such as carboxyl and hydroxyl groups necessary to improve the interfacial adhesion between the adhesive and PET side of the barrier film. The contact angle measurement results of barrier films with different surface

treatments using both water and hexadecane probe liquids, are shown in **Figure 2.5**. These results and calculated surface energies via both harmonic and geometric mean methods using equations (2.1)–(2.3) are listed in **Table 2.1**.

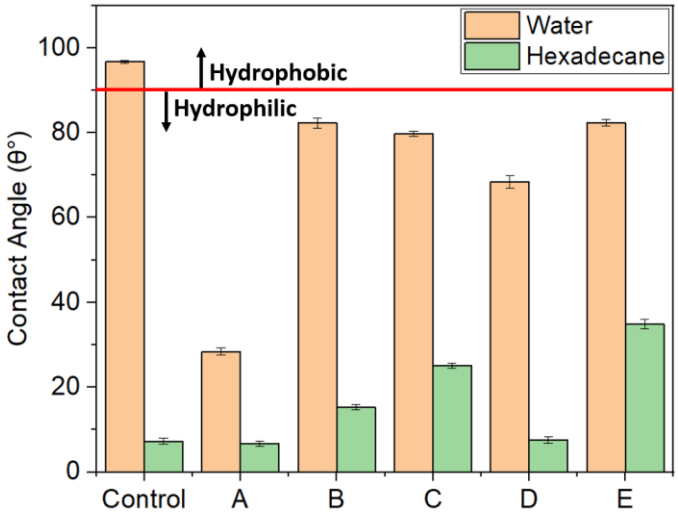

Figure 2.5 Contact angle measurement data of 3M Barrier Film of Treatment A–E.

Table 2.1 Contact angle and surface energy measurements via harmonic (H) and geometric (G) mean methods of barrier films with different types of surface treatment on the 3M Barrier Films.

	Contact Angle (θ°)		Dispersion Component, γ_s^d (mJ/m²)		Polar Component, γ_s^p (mJ/m²)		Surface Energy, γ_s (mJ/m²)	
	Water	*Hexadecane*	*H*	*G*	*H*	*G*	*H*	*G*
Control	96.71 ± 0.34	7.22 ± 0.69	27.38	27.38	4.27	1.17	31.65	28.55
Treatment A (Amine-Silane)	28.44 ± 0.89	6.62 ± 0.60	27.42	27.42	38.87	37.89	66.29	65.31
Treatment B (Epoxy-Silane)	82.32 ± 1.21	15.25 ± 0.60	26.64	26.64	10.41	5.78	37.05	32.42
Treatment C (Vinyl-Silane)	79.73 ± 0.64	25.09 ± 0.60	25.11	25.06	12.09	7.47	37.21	32.53
Treatment D (UV/O_3)	68.40 ± 1.40	7.59 ± 0.81	27.36	27.36	17.03	12.63	44.39	39.99
Treatment E (UV/O_3 + Vinyl)	82.26 ± 0.77	34.81 ± 1.12	23.07	22.88	11.59	7.05	34.66	29.94

In **Figure 2.5** and **Table 2.1**, the contact angle (θ°) of water on the substrate decreases upon the individual treatment. In general, a contact angle greater than 90° is said to be hydrophobic and that lower than 90° as hydrophilic [41, 42], which is differentiated by the red horizontal border line in **Figure 2.5**. Apart from the control sample, all samples of each treatments exhibited hydrophilic characteristics. While the contact angle of the control sample is 96.71° ± 0.34°, that of the sample treated with amine-silane (treatment A) is 28.44° ± 0.89°, which shows the most significant decrease and consequently the lowest water contact angle. Also, hexadecane, although a good probe liquid for contact angle measurement, only has a dispersive component of its surface tension (27.6 mJ/m^2), whereas water has both dispersive and polar components of its surface tension (21.8 and 51.0 mJ/m^2, respectively) [36]. The absence of a polar component for hexadecane could explain the dynamic wetting or dispersion onto the substrate surfaces for the control and samples with treatments A and treatment D, in which their contact angles are 7.22° ± 0.69°, 6.62° ± 0.60°, and 7.59° ± 0.81°, respectively, all well below 10°. Samples with Treatment E have the highest hexadecane contact angle of 34.81° ± 1.12°, which means among all the samples, 3M Barrier Film with the UV/Ozone followed by a vinyl-silane organic treatment will have the lowest wettability of a non-polar liquid.

Surface energies using geometric and harmonic mean methods of the barrier film at different surface treatment techniques are plotted in **Figure 2.6a** and **Figure 2.6b**, respectively, in which they are individually separated into their polar and dispersive components.

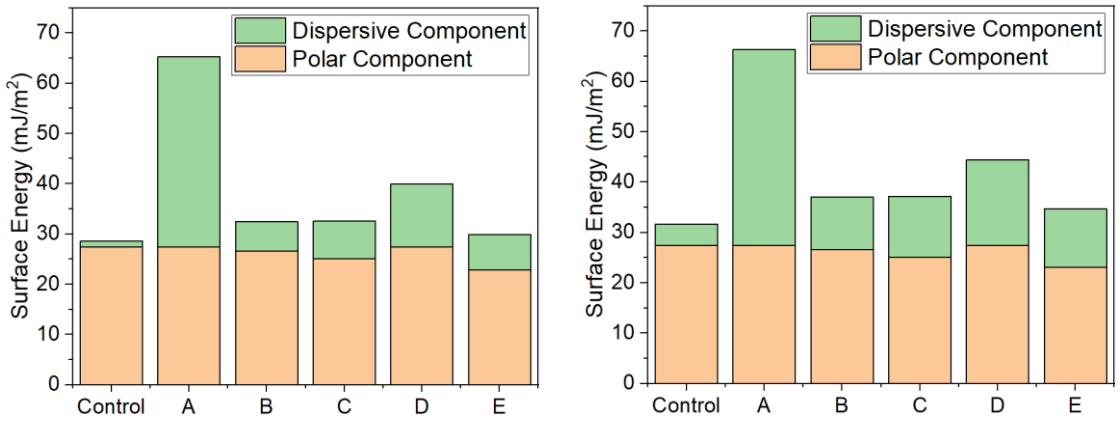

Figure 2.6 Surface energies of 3M Barrier Film with different types of Treatment A–E, broken into their polar and dispersive components using (a) geometric mean method and (b) harmonic mean method.

Surface energies of the control sample using harmonic and geometric mean methods are 31.65 and 28.55 mJ/m^2, respectively, whereas those of samples treated amine-silane are the highest: 66.29 and 65.31 mJ/m^2. Due to the decrease in the water contact angle of the PET with all types of treatment, there is an overall increase of surface energies for all samples with chemical, physical, and both combined treatments. In summary, the surface energy of the samples with Treatment A and Treatment D was 2.2 and 1.4 times greater than that of the control samples without any surface treatment, and at least a 7% increase in surface energy was observed for the surface-treated samples.

In **Figure 2.6**, it is apparent for both geometric and harmonic mean methods that there is a limited relationship between the dispersive components of the surface energies. However, from both the geometric and harmonic mean methods, there is a sudden increase in the polar components. One of the supporting reasons for the overall increase in surface

energy or that of the polar component is the introduction of new functional groups or an increase in the concentration of the already present functional groups on the PET after silane treatment, UV/Ozone treatment, or both. This hypothesis is supported by other literature reports' findings where an introduction of organic functional groups (essential adhesion promoters) on PET films increases their wettability [32, 43]. These findings are based on surface treatment via plasma-etching at two temperature conditions (room temperature, 25 °C and a high temperature, 130 °C), APP jet etching, and UV excimer light, all three of which are more aggressive methods compared to our UV/Ozone physical treatment at room temperature [32, 43]. Therefore, not only the APP jet etching and UV excimer light treatment, but also the weaker UV/Ozone treatment can be used as a method to promote the formation of organic functional groups [34, 35].

2.4 Stability of Test Coupons Designed as Simplified PSC Package

2.4.1 Interfacial Adhesion Strength Prior to Aging Tests

T-peel tests were used to measure the mechanical behavior of the samples with different types of surface treatment including either chemical, UV/ozone, or both. Three different conditions were used to determine the effect of thermal and moisture aging on the interfacial adhesion strength between QSil (PDMS) and the PET substrate of the 3M Barrier Film. The output of this type of test yielded load/displacement curves, and each reported measurement is an average of at least five samples, excluding the maximum and minimum value of peel-off force. **Figure 2.7** illustrate the processed data of T-peel test results prior to aging and is normalized in respect to the control sample for comparison between samples with different treatments to control.

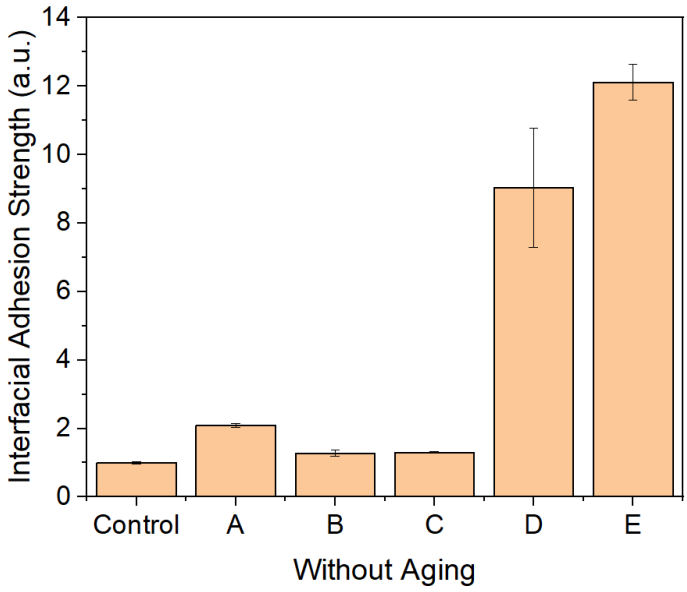

Figure 2.7 Average normalized peel-off force of PDMS adhesive on 3M Barrier Film (PET surface) in respect to control sample prior to aging.

As expected, due to the increase in surface energy, oxygen elemental composition, and hydroxyl and carboxyl functional groups, UV/Ozone treated samples (Treatment E) yielded one of the highest average peel-off force before aging. In addition, samples with Treatment A, showing the highest surface energies among the samples, also increased by 2.1-fold. Surprisingly, samples with Treatment E (UV/ozone + vinyl) were observed with the highest interfacial adhesion strength (12.1-fold increase), which was not supported by our earlier surface energy calculations. The exact explanation for this phenomenon, a linearity between the surface energy and the interfacial adhesion strength, was not available.

2.4.2 Moisture and Thermal (Damp-Heat) Stability of Test Coupons

To study the effects of temperature and relative humidity on adhesion strength, samples were aged at 60 °C/Dry and 60°C/90% R.H. For a good PV module packaging system, maintaining high adhesion in damp heat conditions is favorable. **Figure 2.8a** illustrates the effect of thermal temperature on the surface-treated PET side of the barrier film, and **Figure 2.8b** illustrates the effect of damp-heat environment on the samples. Note from both figures that all surface-treated samples retained higher interfacial adhesion strength than the control sample. From thermal aging, samples with Treatment D had the highest interfacial adhesion strength, up to 2.01 times higher (**Figure 2.8a**), whereas from thermal and moisture aging, samples with Treatment A had the highest interfacial adhesion strength, up to 2.03 times higher (**Figure 2.8b**).

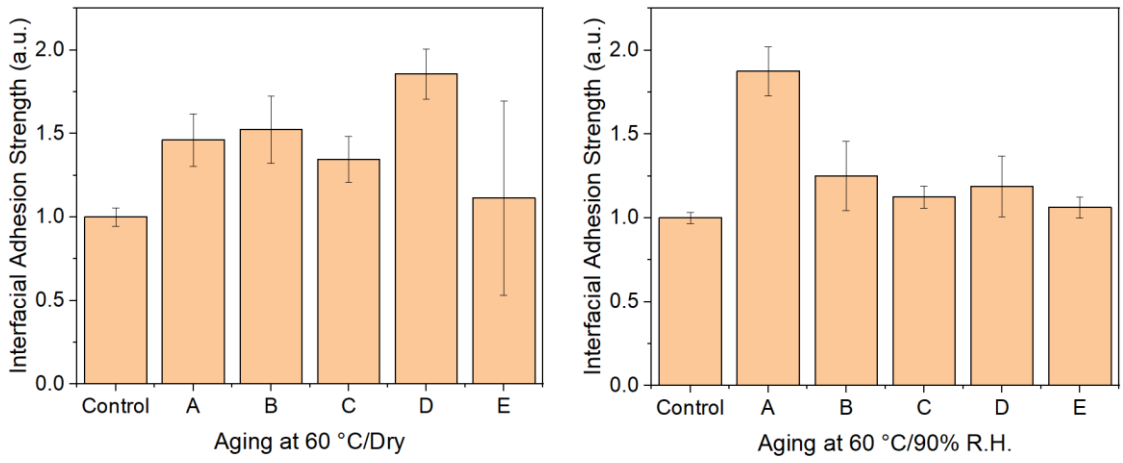

(a) (b)

Figure 2.8 Average normalized peel-off force of PDMS adhesive on 3M Barrier Film (PET surface) in respect to control sample: (a) aging at 60 °C/Dry condition for 8 hours and (b) aging at 60 °C/90% R.H. condition for 8 hours.

Figure 2.9 illustrates the true average values of the interfacial adhesion strength of all samples at two different aging conditions. Note that samples with Treatment D and E yielded the highest initial interfacial adhesion strength between the barrier adhesive and the PET side of the barrier film. Though their adhesion strengths were the highest, after aging under either elevated temperature or both elevated temperature and high humidity, their adhesion strengths decreased significantly. Noticeably, samples with Treatment A were the least susceptible to temperature and high humidity. To further understand the thermal and moisture stability and their behavior, interfaces of the samples upon treatment were characterized using FTIR.

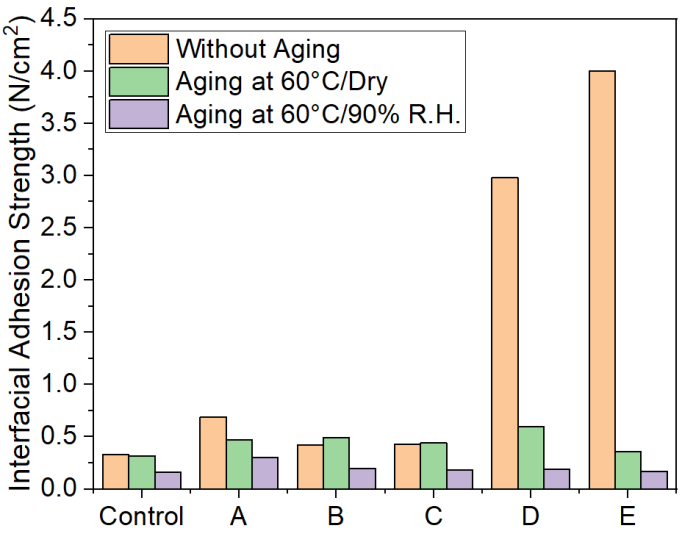

Figure 2.9 Combined results of average peel-off force of PDMS adhesive on 3M Barrier Film (PET surface) per different aging conditions.

2.5 Interface Characterization via FTIR Characterization

FTIR spectra (**Figure 2.10**) were obtained to verify the presence of the functionalized silanes on PET and of the formation of new functional groups upon chemical treatment of

PET, before deposition of the coupling agents. An ethanolic solution of hydrolyzed APTES is reported to have N-H stretching vibrations at 3368 cm^{-1} and 3295 cm^{-1}, and bending vibrations at 1567 cm^{-1} and 1486 cm^{-1} [44]. The presence of APTES on the PET is confirmed in **Figure 2.10a** by the observed peaks at 3364 cm^{-1}, 3290 cm^{-1}, 1560 cm^{-1}, and 1487 cm^{-1}. **Figure 2.10b** is illustrated to confirm functional groups formed by Treatment E, which resulted from interaction between oxygen from carboxyl, carbonyl, and hydroxyl groups on the PET substrate upon UV/Ozone treatment and hydrolyzed-VTMS, specifically the $Si(OH)_3$ group. Hydrogen bonding interactions are present between the two groups, which is illustrated by the broad O-H stretching vibrations around 3300 cm^{-1}.

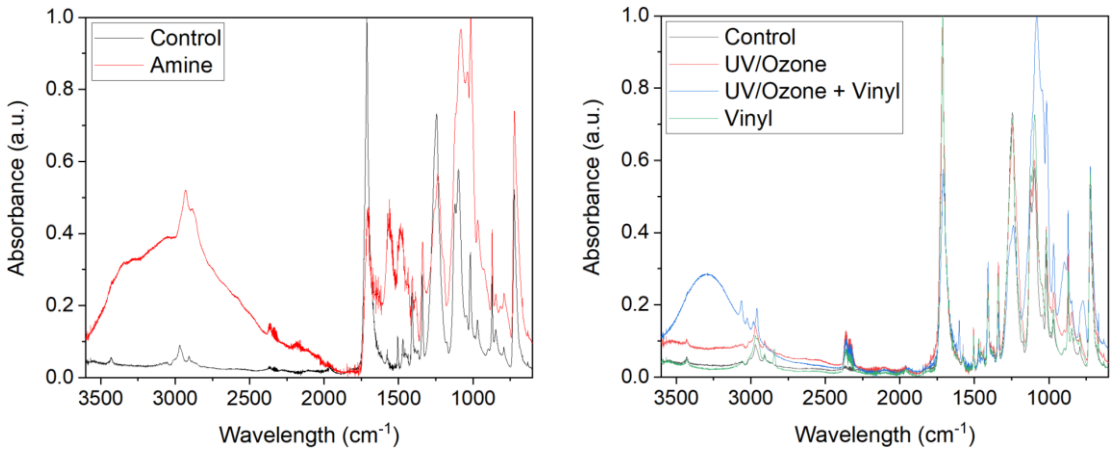

(a) (b)

Figure 2.10 FTIR-ATR spectrum at interface of PET film upon treatment: (a) Control and Treatment A and (b) Control, Treatment C, Treatment D, and Treatment E.

From sum frequency generation studies at PET/silane interfaces, [45] hydrolyzed $Si(OH)_3$ groups were available for the bulk polymer with APTES-functionalized PET as NH_2 groups were oriented towards the PET surface. Usually, trialkoxy groups in silane coupling agents tend to bond to an inorganic substrate surface while the functionalized end

groups tend to bond to the polymer adhesive [45]. However, this is not the case for all silane coupling agents, and in fact, it has been suggested that some end groups such as hydrolyzed-APTES interact with the inorganic substrate surfaces [46]. Based on this study, we also assume that the NH_2 groups in the APTES in our samples are oriented towards the PET surface. This assumed the orientation may explain why we observe the lowest peel strength degradation for Sample A upon damp-heat aging (**Figure 2.8b**). The formation of hydrogen bonds from interaction between amino end groups in ATPES molecules and the carbonyl oxygens on the PET surface could explain the relatively lower peel strength degradation upon aging [45]. We then assume that GPTMS and VTMS coupling agents are not oriented in the same way as APTES, as no interaction between epoxy and butyl end groups was observed with carbonyl oxygens on the PET surface [45], meaning the $Si(OH)_3$ groups are oriented towards the PET surface and the functionalized ends are oriented away from the surface and towards the PDMS. This leaves the epoxy and vinyl groups available to "bind" to the PDMS adhesive. The T-peel test showed that samples modified with Treatment B and Treatment C had higher peel strength degradation than samples modified with Treatment A.

Our earlier study suggests interfacial bonding between the PDMS adhesive and the barrier film was enhanced and verified by T- peel tests [35]; there was a 15.8% increase in the peak peel-off force and 28.3% increase in the average peel-off force. This result was verified by X-ray Photoelectron Spectroscopy (XPS) and its deconvolution of C 1s peaks, in which relatively more hydroxyl (12.39% area) and carboxyl (9.49% area) components were observed for samples with Treatment D and only 2.26% area and 2.86% area, respectively were observed for the control (untreated) sample. This finding is explained in

series. Ozone undergoes a decomposition reaction by a thermal reaction: $O_3 \longrightarrow O_2 + O$ [47]. Also, ozone treatment of hydrocarbons (that reside on the PET surface) leads to the formation of intermediate radicals and decomposition into molecular oxygen and hydroxyl radicals [48-50]. Therefore, UV on ozone treatment further induces thermal decomposition of ozone or enhances oxidative reactions. These reactions generate radicals, which then decompose into functional groups that bind to the polymer surface, resulting in an increase in the relative concentration of carboxyl groups. This leads to an increase in the interfacial bonding and cohesive failure of PDMS, which was observed in T-peel tests for results (**Figure 2.7**). Due to this result that shows an increase in hydroxyl and carboxyl groups, Treatment E was performed, which yielded the highest adhesion strength (**Figure 2.7** and **Figure 2.9**). The highest adhesion strength could also be explained due to the strong hydrogen bond formation between three OH groups per hydrolyzed-VTMS molecule and hydroxyl- and carboxyl-groups rich on the surface of PET upon UV/Ozone treatment. In addition, the vinyl-silane head groups are available for strong chemical bonding with silanol backbone in PDMS adhesive. The result in **Figure 2.7** can be therefore explained from the strong hydrogen bonding between the PET and the hydrolyzed-VTMS and strong silane linkage between the hydrolyzed-VTMS and the PDMS adhesive. Also, it is observed in many cases that hydrogen bonding, and acid-base type of bonds, between the substrate and polymer could enhance physical adhesion [51-53]. However, their adhesion strength was dramatically affected upon aging. Although hydrogen bonding promotes stronger adhesion between the substrate and the polymer, it does not suffice as the sole mechanism of bonding for environmentally stable adhesion, such as in damp-heat condition as observed in this study. Also, it is possible that at high temperature, moisture can induce

hydrolysis reaction, which can potentially break in-situ hydrogen bonding as hydrogen bonding interaction is not durable neither in a heated nor in a damp condition [53].

2.6 Summary

Chemical, UV/Ozone, and combined surface treatments on a PET substrate were studied and shown to promote stronger interfacial adhesion that delays moisture ingress through the interface between a silicone adhesive and PET substrate. This type of interface engineering is a crucial study as PSCs are highly moisture-sensitive. Although a barrier film can block moisture in the transverse direction, moisture can still penetrate from the lateral sides of the PV modules, which include the interfaces. To increase their interfacial adhesion strength, we proposed a combined surface treatment comprised of UV/Ozone treatment followed by a VTMS chemical treatment. From our T-peel test data, PET substrates with Treatment E showed the highest enhancement in adhesion strength, a 12.1-fold increase, with the PDMS adhesive. However, treated surfaces that showed enhanced adhesion strength lost this enhancement upon damp/heat aging test as they showed no significant difference compared to the control sample. However, with Treatment A, the interfacial adhesion strength was still two times better than the control sample. This finding was supported by FTIR-characterization and comparison between the peel-test results and the literature reviews [45, 46]. Although hydrogen bonding was observed in samples with Treatment A and Treatment E, samples with Treatment E degraded under damp/heat environment due to the higher susceptibility to moisture on hydrogen bonds between $Si(OH)_3$ and oxygen from carbonyl group on the PET.

On the other hand, the bonding of NH_2 and oxygen from the carbonyl group on the PET is much stronger at a damp/heat environment. It is difficult to conclude which interface is responsible for relatively "stronger adhesion". Therefore, one cannot make assertions on the orientation of the coupling agent based on a peel test. Also, and more importantly, there is definitely more than one layer of coupling agent on the PET, so it does not matter how the first layer is oriented on PET. Yet, due to the multi-layers of coupling agents on the PET film, the assertion one can make would be in relation to the relative polarities among the isolated compounds and how that affects the interfacial adhesion strength on both sides (coupling agent/PET and coupling agent/PDMS). Based on these findings from this study, employing inorganic surface modification such as Si_3N_4 plasma-enhanced chemical vapor deposition (PECVD) that generates much stronger covalent bonds will be explored in the future.

CHAPTER 3. UV, THERMAL, AND MOISTURE DEGRADATION OF THERMALLY-CURED EVA ENCAPSULANT

3.1 Introduction

Many studies have explored on the degradation profiles of solar cell encapsulant materials. For example, Cai et. al. studied the effect of UV aging on thermally-cured silicone encapsulant adhered to borosilicate glass [54]. Also, Jorgensen et. al. studied the effect of UV and damp-heat aging on thermally-cured EVA encapsulant adhered to glass and PET substrates [55]. However, there still lacks a comprehensive study that relates between the adhesion behaviour upon different degradation tests and the surface chemistry of the delaminated samples that are UV, thermally, and damp-heat exposed samples. Many literatures provide adhesion behaviours but does not interpret the results in relation to its surface chemistry. This chapter analyses the mechanical test results of the delaminated PET-EVA-PET encapsulated test coupons and discusses the surface and interface chemistry of the delaminated PET-EVA samples via XPS characterization and its thorough analyses.

3.2 Experimental

3.2.1 Materials

A commercial, potential induced degradation (PID) resistant EVA copolymer PV encapsulating film (PHOTOCAP 15580P) was purchased from STR, and a commercial

heat-stabilized and pretreated 125 μm thick PET film (MELINEX ST505) was purchased from DuPont Teijin Films. **Table 3.1** summarizes the materials used in this study and shows the optical transmittance value, one of the important factors earlier mentioned in **Figure 1.3.**

Table 3.1 Optical transmittance of the materials used in this study.

Materials	Manufacturer	Model	Optical Transmittance
EVA Copolymer	STR	PHOTOCAP 15580P	91%
PET Backsheet	DuPont	MELINEX ST505	88%

3.2.2 Sample Fabrication and Aging Conditions

The EVA film was sandwiched between the two ST505 PET films and hot pressed at 140 °C for 8 minutes with 15 bar of applied pressure, which is a recommended curing profile from the manufacturers. The exact lamination profile of PET-EVA-PET sandwich is illustrated in **Figure 3.1**, in which the sample fabrication was achieved in collaboration with M. Sulkis [56]. This sample was cut into long strips with 1 cm in width (**Figure 3.2**) for T-peel test as a mechanical characterization to understand the adhesion behaviour upon different aging conditions.

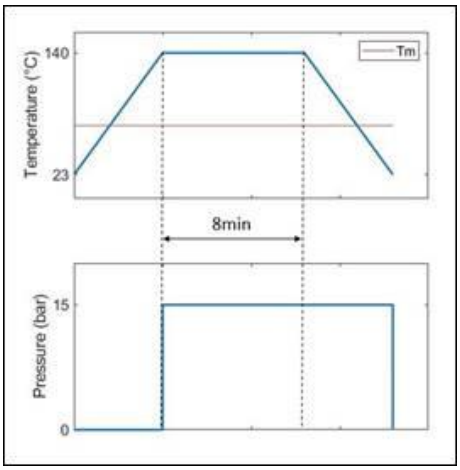

Figure 3.1 Curing and lamination profiles for thermally-cured EVA. In collaboration with M. Sulkis [56].

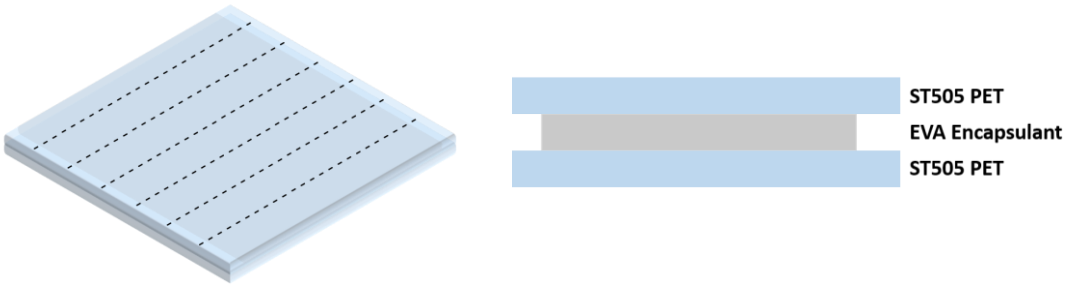

Figure 3.2 Schematic of PET-EVA-PET samples for aging tests. Note that the actual appearance is colorless and optically transparent.

To study the effects of UV exposure on encapsulated test coupons that resembles the PV module packages, as-prepared samples seen in **Figure 3.2** were aged in an ELC-4001 UV flood system (Electro-Lite Corporation, Bethel, CT) for UV aging test. The power of the UV lamp was measured to be 832 W/m^2 and was peaked at ~365 nm. The spectral irradiance at the bottom of the UV system was measured using a Jaz spectrometer by Ocean Optics and is illustrated in **Figure 3.3a**. The entire set of samples were allocated

to make sure all were exposed to the UV (**Figure 3.3b**). The sample surface temperature was measured to be ~65 °C during UV irradiation. To evaluate any effect on this temperature on the samples, thermal aging at 65 °C was also carried out in this experiment. Lastly, a damp-heat accelerated aging test was conducted as well. For these, a bench top environmental chamber (MicroClimate, Cincinnati SubZero, Inc.) was used to at the samples at 65 °C for thermal aging and 85 °C/85% R. H. for damp-heat aging. Please note that the aging tests were conducted in collaboration with M. Sulkis [56].

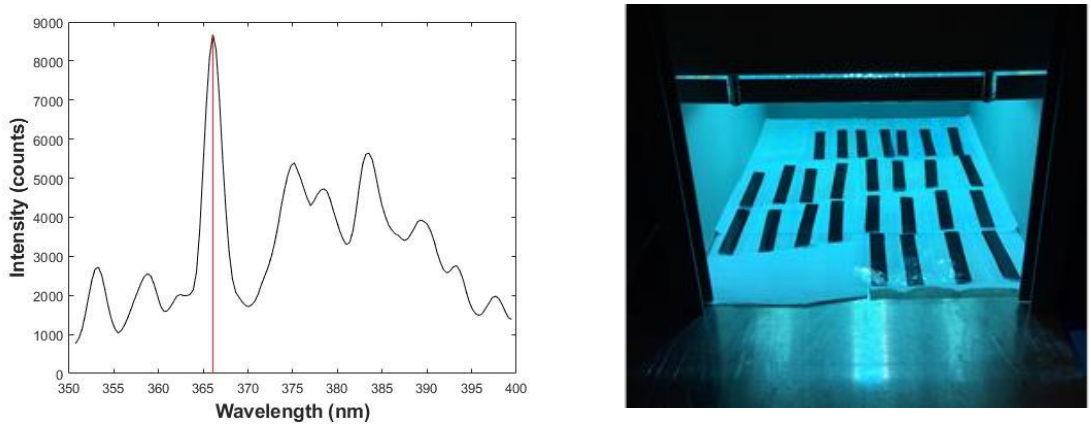

(a) (b)

Figure 3.3 (a) Spectral irradiance at the surface of the samples determined using a spectrometer and (b) samples under the UV irradiation. Note that these samples are fabricated using different type of encapsulant material. In collaboration with M. Sulkis [56].

Figure 3.4 Schematic of environmental chamber used to thermally and damp-heat age the samples. In collaboration with M. Sulkis [56].

3.2.3 T-Peel Tests

A Universal Testing Machine (Test Resources, Shakopee, MN) was used to perform displacement-controlled T-peel experiments at 100 mm/minute. The same test condition and set-up were used from Chapter 2 (refer to **Figure 2.4**).

3.2.4 X-ray Photoelectron Spectroscopy (XPS) Characterization

The XPS analysis was performed using a Thermo K-Alpha instrument with a monochromatic Al Kα X-ray source ($h\nu$ = 1486.6 eV), 400 μm spot size, and 15 W X-ray gun power. Charge correction was made to all the peaks using the C 1s peak at 285.0 eV. Casa XPS software was used to generate the curves using a Shirley background and Lorentzian–Gaussian (GL30) line shape fitting models.

3.3 Interface Chemistry between PET-EVA prior to Aging Tests

It is reported from Jorgensen et. al. [55], that STR's EVA copolymer contains an adhesion-promoting silane coupling agent. This behavior was also observed from our XPS

analysis and can be seen in, **Figure 3.5**, in which 3.2% of Si was measured from the detected region on the EVA surface. This Si is from the reactive silane coupling agent, one of the additives that are added for EVA formulation (**Table 1.3**). The recent review paper also reports that trialkoxy silane is typically used as a silane additive for EVA [2]. Also, silane coupling agent is widely known and used as a bridging agent to promote adhesion between the two dissimilar materials (i.e. organic and inorganic materials) [57, 58].

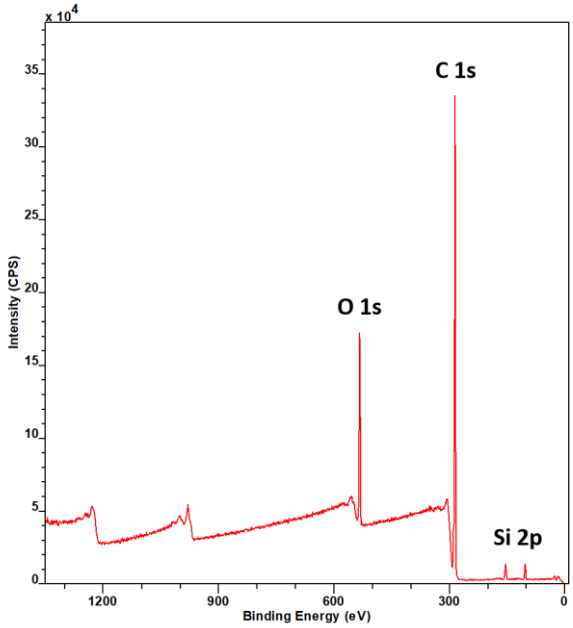

Figure 3.5 XPS survey spectrum of STR PHOTOCAP® 15580P EVA surface.

The PET used in this study is pre-treated using a primer which increases the surface energy and the reactive sites (functional groups) for promoting adhesion. To determine the functional groups residing on this PET surface, XPS analysis was performed. **Figure 3.6** shows a survey spectrum of ST505 PET, which contains the N 1s peak as well. We assumed that this N 1s peak was from the pre-treatment done on this PET surface by the manufacturer. The calculated O/C ratio, N/C ratio, and (O+N)/C ratio were 0.35, 0.03, and

0.38, respectively, which means that the oxygen-containing functional groups (i.e. species) are by 10-fold more dominant than nitrogen-containing species. To determine the specific functional groups, individual C 1s, O 1s, and N 1s peaks were deconvoluted, and their curves are illustrated in **Figure 3.7** with their results summarized in **Table 3.2**.

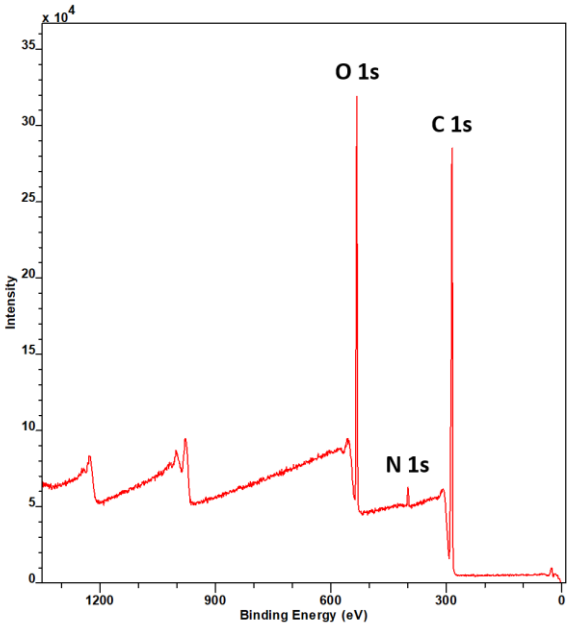

Figure 3.6. XPS survey spectrum of DuPont MELINEX® ST505 PET surface.

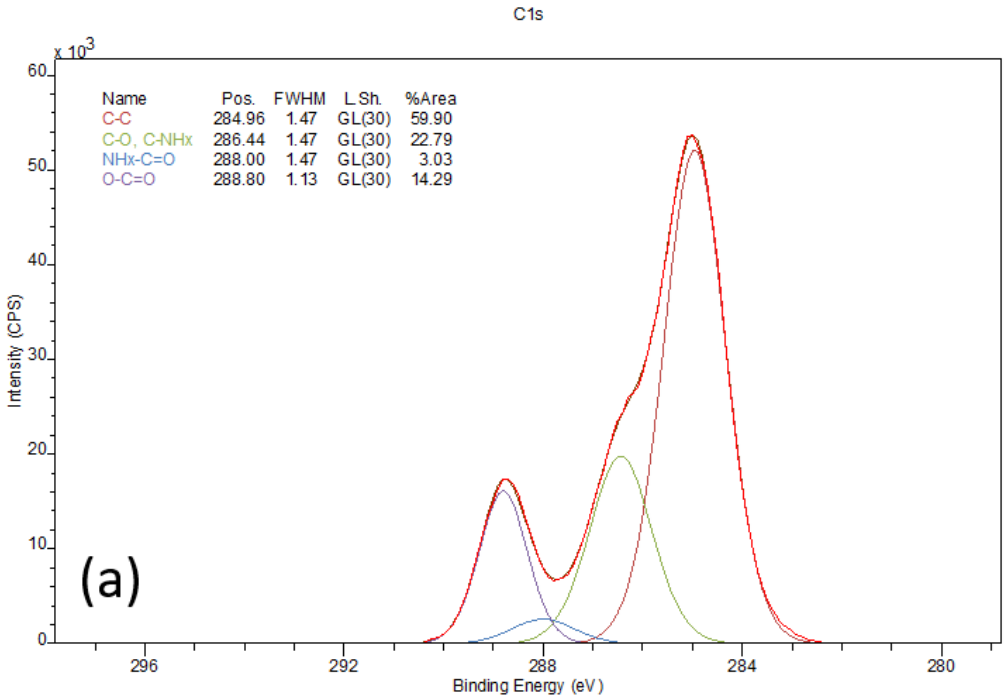
C1s
x 10^3
Name Pos. FWHM L.Sh. %Area
C-C 284.96 1.47 GL(30) 59.90
C-O, C-NHx 286.44 1.47 GL(30) 22.79
NHx-C=O 288.00 1.47 GL(30) 3.03
O-C=O 288.80 1.13 GL(30) 14.29
(a)
Intensity (CPS)
Binding Energy (eV)

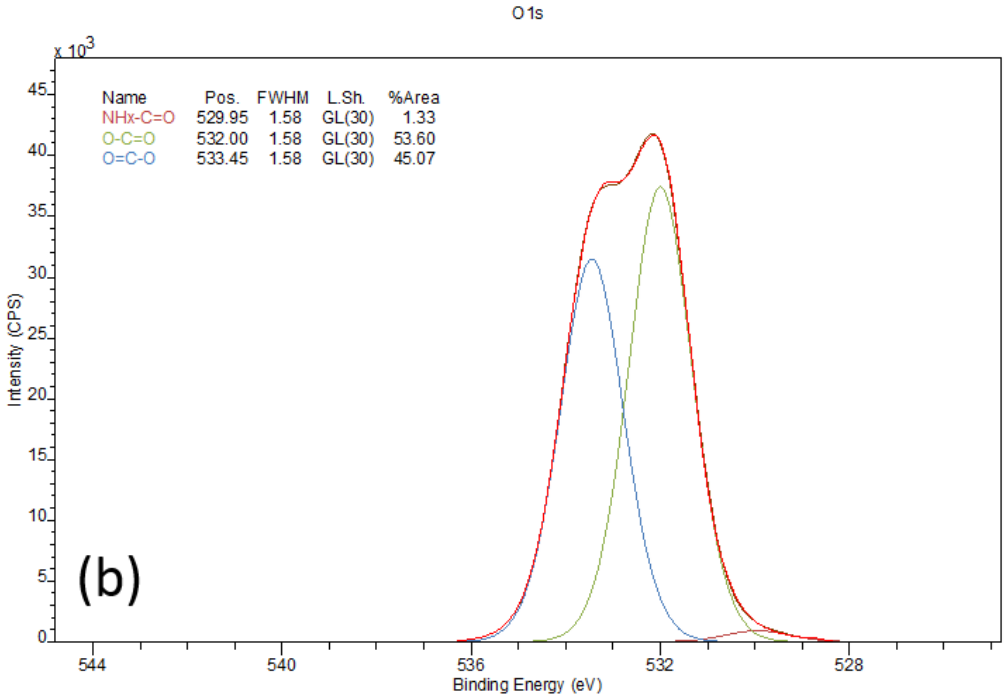
O1s
x 10^3
Name Pos. FWHM L.Sh. %Area
NHx-C=O 529.95 1.58 GL(30) 1.33
O-C=O 532.00 1.58 GL(30) 53.60
O=C-O 533.45 1.58 GL(30) 45.07
(b)
Intensity (CPS)
Binding Energy (eV)

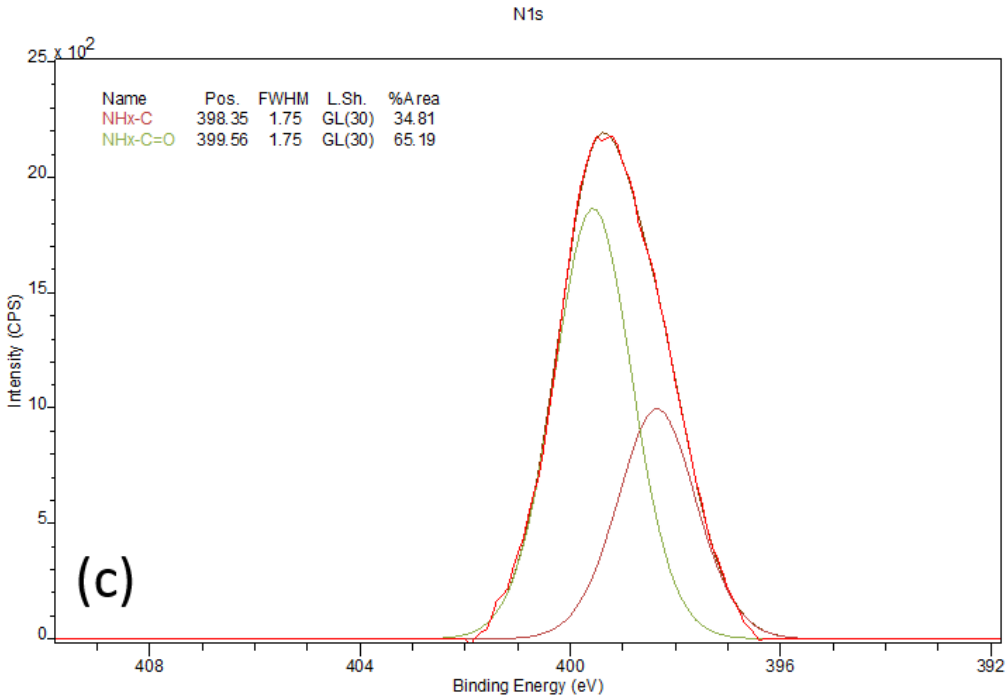

Figure 3.7 XPS spectra of ST505 PET surface with deconvoluted peaks: (a) C 1s, (b) O 1s, and (c) N 1s.

Table 3.2 Average binding energies and full width half max (FWHM) of C 1s, O 1s, and N 1s spectra of ST505 PET surfaces.

		Components	Binding Energy (eV)	FWHM (a.u.)	Area (%)
C1s	**A**	C-C, C-H	285.0 ± 0.02	1.48 ± 0.02	60.36 ± 0.21
	B	C-O, C-NH*x*	286.5 ± 0.04	1.48 ± 0.02	22.07 ± 0.32
	C	NH*x*-C=O	288.0 ± 0.00	1.48 ± 0.02	2.08 ± 0.41
	D	O-C=O	288.8 ± 0.01	1.15 ± 0.02	15.49 ± 0.53
O1s	**A**	NH*x*-C=O	530.1 ± 0.07	1.56 ± 0.01	1.20 ± 0.06
	B	O=C-O	532.0 ± 0.00	1.56 ± 0.01	52.59 ± 0.44
	C	O-C=O	533.5 ± 0.01	1.56 ± 0.01	46.21 ± 0.50
N1s	**A**	NH*x*-C	398.4 ± 0.06	1.77 ± 0.01	35.05 ± 0.47
	B	NH*x*-C=O	399.6 ± 0.06	1.77 ± 0.01	64.95 ± 0.47

Deconvolution of C 1s spectrum yielded the component peaks, which was fitted by fixing the FWHM. However, note that FWHM for the fourth component in C 1s spectrum is not identical with other three values. For C 1s spectrum, best fitting was obtained using this four-component fitting, and it was necessary to not fix the FWHM for Component D to obtain the best fitting. This could be explained due to the fact that C-O and C-NH*x* have overlapping regions, and it is very hard to distinguish these two peaks [59-61]. In addition, the nitrogen containing functional groups such as C=N and C≡N are excluded in **Figure 3.7a**, which should be also considered. Many literature reports that C-N, C=N, and C≡N are positioned close to one another [62-64], which makes the deconvolution and quantification of C 1s extremely difficult [60]. Therefore, it is possible that including all these peaks to deconvolute C 1s spectrum is possible and would fit the curves with uniform FWHM as fitting more curves decreases the FWHM; however, this would make the interpretation very difficult. Nevertheless, from the obtained data, the PET surface was present with -OH, -OOH, and relatively smaller percentage of -NH*x*-C and -NH*x*-C=O. Schematic of PET surface with functional groups as a reacting site for the adhesive is illustrated in **Figure 3.8**.

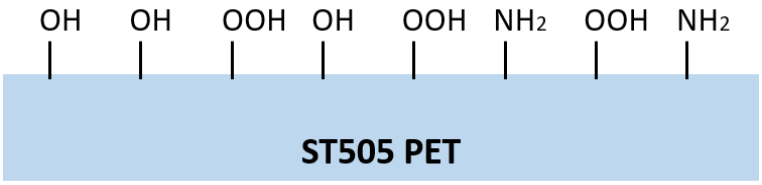

Figure 3.8 Schematic representative of ST505 PET surface with reactive sites for adhesion with EVA.

Combining the EVA and PET interface structures together, **Figure 3.9** illustrates the possible interface formed during lamination of EVA onto the PET.

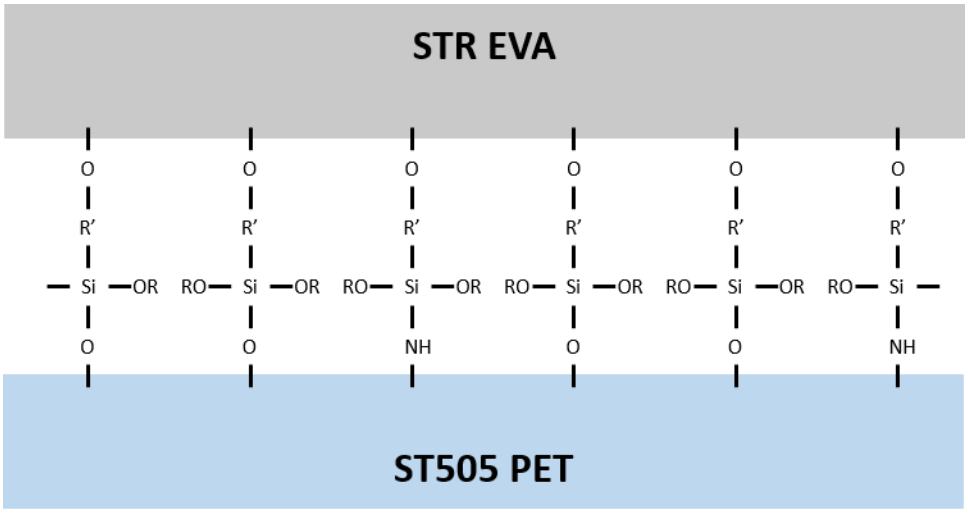

Figure 3.9 Schematic representative of the possible interface network between the ST505 PET and the STR EVA, where –OR represents –(OCH_3) and –R'– represents –$CH_2CH(CH_3)CO_2(CH_2)_3$)– groups.

3.4 Degradation Profiles of PET-EVA Interface at Different Aging Conditions

3.4.1 Effect of UV Aging on the PET-EVA Adhesion Chemistry

The interfacial adhesion strength between the ST505 PET and EVA of PET-EVA-PET sandwiched samples is depicted in **Figure 3.10** (in collaboration with M. Sulkis [56]). Samples exposed to a few hours of UV ($t_{1.5}$ and t_3) had higher peel strengths than untreated (t_0) samples. However, samples with >8h of UV exposure (t_{16}, t_{20}, t_{24}, t_{48}) had drastically lower peel strengths, which indicated that there was degradation either at the sample interface, bulk, or both.

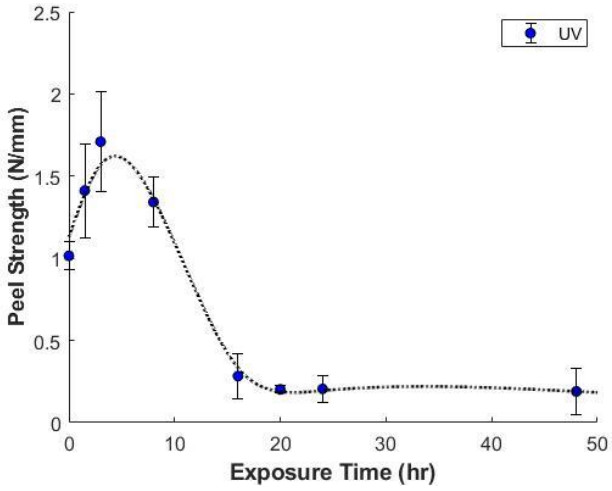

Figure 3.10 T-Peel test characterization of PET-EVA-PET sample upon UV aging at 365 nm. In collaboration with M. Sulkis [56].

To further investigate the cause of delamination, the surface of the peeled EVA was examined using a Leica digital microscope, results shown in **Figure 3.11** (in collaboration with M. Sulkis [56]). A set of $t_{1.5}$ samples demonstrated cavitation (**Figure 3.11a**), while a set of t_{24} sample did not (**Figure 3.11b**). In summary, we observed that samples that were exposed to UV for a few hours ($t_{1.5}$ and t_3), delaminated with cavitation (stickier) and with higher peel strengths than samples without UV exposure (t_0), and samples with prolonged exposure (>t_8). We therefore characterized the chemical composition of the peeled surfaces with XPS to understand the interface chemistry and further enhance the analysis.

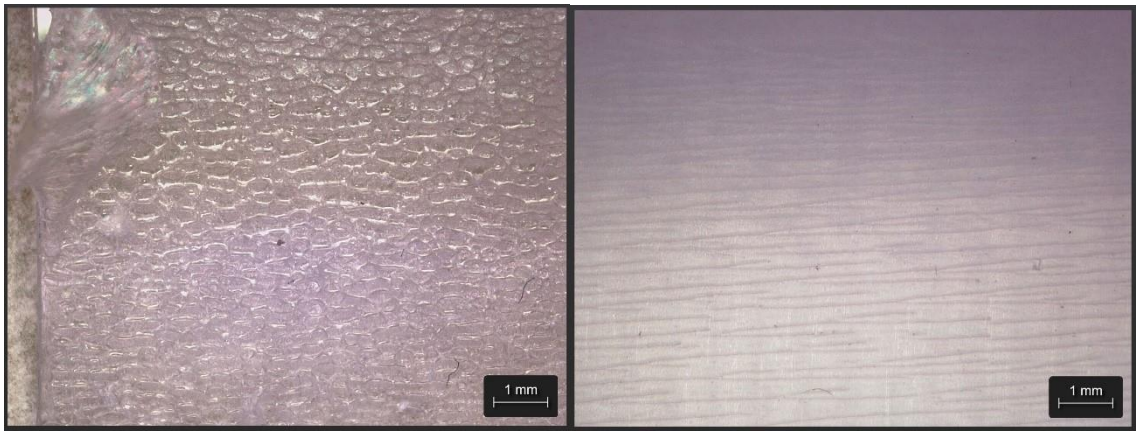

(a) (b)

Figure 3.11 Delaminated surface of the EVA side upon T-Peel mechanical test: (a) delamination with cavitation for a sample exposed to 1.5 h of UV and (b) delamination without cavitation for a sample exposed to 24 h of UV. In collaboration with M. Sulkis [56].

Table 3.3 summarizes the detected elemental peaks of delaminated PET surfaces from UV aged samples ($t_{1.5}$ and t_{24}) compared against the surface of a control sample (t_0) without UV exposure. These data were calculated from the survey spectra and represents an average of 5 points on the surface. While C 1s, O 1s, and Si 2p peaks were present in all samples, the N 1s peak was only identified for the control and sample $t_{1.5}$. In addition, the N 1s peak was also not detected on the EVA side. Therefore, the most probable bond cleavage site for the t_{24} sample is at the R'-Si bond as illustrated in **Figure 3.12**. There is a possibility that prolonged UV exposure on the t_{24} sample could have generated volatile species; however, this assumption was not supported as 51.01 ± 0.89% of Si-N and 47.93 ± 0.80% of N-Si-O bonds were present on the PET side of the t_{24} sample, from the deconvolution of Si 2p spectra (**Table 3.4**).

Table 3.3 Average elemental composition from survey spectra of ST505 PET surfaces of delaminated T-Peel samples upon UV aging at 365 nm and its O/C ratio.

		t_0	$t_{1.5}$	t_{24}
Element (%)	**C 1s**	73.97 ± 0.92	75.07 ± 0.54	74.01 ± 0.17
	O 1s	22.37 ± 0.95	21.39 ± 0.39	25.06 ± 0.19
	Si 2p	1.31 ± 0.19	1.32 ± 0.14	0.94 ± 0.19
	N 1s	2.35 ± 0.15	2.21 ± 0.15	Undetected
	O/C Ratio	0.30	0.28	0.34

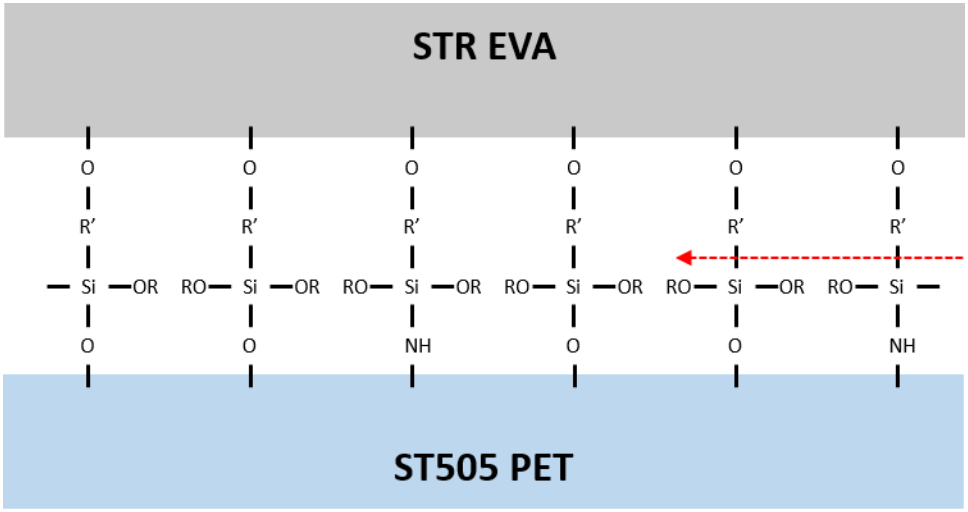

Figure 3.12 Proposed bond cleavage region for t_{24} sample.

Table 3.4 Average binding energies and full width half maxima (FWHM) of C 1s, O 1s, Si 2p, N 1s spectra of ST505 PET surfaces of delaminated T-Peel Samples upon UV aging at 365 nm.

			Components	Binding Energy (eV)	FWHM	Area (%)
t_0	C 1s	A	C-Si	283.0 ± 0.1	1.48 ± 0.02	1.17 ± 0.05
		B	C-C, C-H	285.0 ± 0.1	1.48 ± 0.02	66.29 ± 2.08
		C	C-O, C-NH*x*	286.6 ± 0.1	1.48 ± 0.02	17.09 ± 1.23
		D	NH*x*-C=O	287.7 ± 0.1	1.48 ± 0.02	2.12 ± 0.15
		E	O-C=O	288.9 ± 0.1	1.23 ± 0.01	13.34 ± 0.98
	O 1s	A	NH*x*-C=O	530.2 ± 0.1	1.55 ± 0.01	2.25 ± 0.63
		B	O=C-O	532.1 ± 0.1	1.55 ± 0.01	55.62 ± 1.07
		C	O-C=O	533.6 ± 0.1	1.55 ± 0.01	42.13 ± 1.67
	Si 2p	A	Si-C	100.2 ± 0.2	1.74 ± 0.06	1.27 ± 0.34
		B	Si-N	101.8 ± 0.1	1.74 ± 0.06	26.10 ± 3.13
		C	N-Si-O	102.6 ± 0.1	1.74 ± 0.06	49.10 ± 1.81
		D	Si-O	103.5 ± 0.1	1.74 ± 0.06	25.53 ± 2.52
	N 1s	A	N-Si	397.9 ± 0.1	2.18 ± 0.05	2.02 ± 1.43
		B	NH*x*-C	398.6 ± 0.1	2.18 ± 0.05	44.53 ± 1.09
		C	NH*x*-C=O	399.9 ± 0.1	2.18 ± 0.05	53.46 ± 1.58
$t_{1.5}$	C 1s	A	C-Si	283.0 ± 0.1	1.48 ± 0.02	1.14 ± 0.05
		B	C-C, C-H	285.0 ± 0.1	1.48 ± 0.02	67.04 ± 1.43
		C	C-O, C-NH*x*	286.6 ± 0.1	1.48 ± 0.02	16.85 ± 1.01
		D	NH*x*-C=O	287.7 ± 0.1	1.48 ± 0.02	2.17 ± 0.28
		E	O-C=O	289.0 ± 0.1	1.26 ± 0.03	12.79 ± 0.24
	O 1s	A	NH*x*-C=O	530.3 ± 0.1	1.56 ± 0.03	2.22 ± 0.60
		B	O=C-O	532.1 ± 0.1	1.56 ± 0.03	55.43 ± 0.35
		C	O-C=O	533.6 ± 0.1	1.56 ± 0.03	42.35 ± 0.89
	Si 2p	A	Si-C	99.6 ± 0.1	1.76 ± 0.10	1.49 ± 0.81
		B	Si-N	101.9 ± 0.1	1.76 ± 0.10	37.11 ± 1.81
		C	N-Si-O	102.7 ± 0.1	1.76 ± 0.10	47.92 ± 0.92
		D	Si-O	103.6 ± 0.1	1.76 ± 0.10	13.48 ± 1.71
	N 1s	A	N-Si	397.9 ± 0.1	2.26 ± 0.08	2.73 ± 2.06
		B	NH*x*-C	398.6 ± 0.1	2.26 ± 0.08	41.35 ± 2.46
		C	NH*x*-C=O	400.0 ± 0.1	2.26 ± 0.08	55.92 ± 0.61
t_{24}	C 1s	A	C-Si	283.4 ± 0.1	1.27 ± 0.01	2.23 ± 0.03
		B	C-C, C-H	285.0 ± 0.1	1.27 ± 0.01	63.64 ± 0.43
		C	C-O, C-NH*x*	286.7 ± 0.1	1.27 ± 0.01	17.52 ± 0.14
		D	NH*x*-C=O	287.8 ± 0.1	1.27 ± 0.01	Undetected
		E	O-C=O	289.0 ± 0.1	1.03 ± 0.01	14.65 ± 0.15
		F	π-π* shake-up	291.5 ± 0.1	1.96 ± 0.09	1.96 ± 0.16
	O 1s	A	NH*x*-C=O	530.0 ± 0.1	1.41 ± 0.01	1.00 ± 0.08
		B	O=C-O	532.0 ± 0.1	1.41 ± 0.01	50.88 ± 0.38
		C	O-C=O	533.6 ± 0.1	1.41 ± 0.01	48.12 ± 0.44
	Si 2p	A	Si-C	100.1 ± 0.2	1.57 ± 0.06	0.87 ± 0.52
		B	Si-N	101.8 ± 0.1	1.57 ± 0.06	51.01 ± 0.89
		C	N-Si-O	102.6 ± 0.1	1.57 ± 0.06	47.93 ± 0.80
		D	Si-O	104.0 ± 0.1	1.57 ± 0.06	0.18 ± 0.20

It was observed that the adhesion strength of $t_{1.5}$ samples was greater than that of t_0 samples. There is also a decrease in oxygen content from the t_0 sample to the $t_{1.5}$ sample, thus a decrease in the O/C ratio from 0.30 to 0.28 (**Table 3.3**). Usually, UV irradiation on PET leads to an increase in the O/C ratio, which was observed in a study performed by Uchida and co-workers [65]. They found that UV irradiation for 2 h was sufficient for saturation of surface oxidation on the PET film [65]. However, the decrease in O/C ratio for the $t_{1.5}$ sample could also be explained by photopolymerization. **Figure 3.13** illustrates potential pathways for polymerization and oxidation upon UV irradiation on the PET-EVA interface. It is known that the PET side is oxidized upon UV irradiation. This oxygen content at the PET surface is progressively consumed by EVA polymer radicals that are also formed from UV irradiation [66]. Therefore, it is probable that radicals form on the PET side from UV as the PET surface consumes more oxygen to form more interfacial bonds with the unreacted surface bonds and radicals from the EVA.

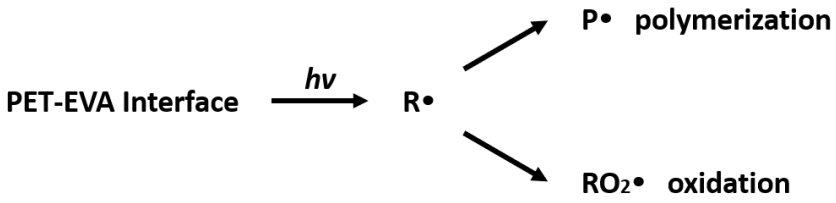

Figure 3.13 Pathway for polymerization at the PET-EVA interface and oxidation on each surface.

The components deconvoluted from the C 1s and O 1s spectra show that there is a similar area % between the t_0 and $t_{1.5}$ samples. However, from deconvolution of the Si 2p spectra, the UV-irradiated $t_{1.5}$ samples had a lesser amount of Si-O component than the t_0 samples, but the $t_{1.5}$ samples had a higher Si-N component than the t_0 samples. These

phenomena demonstrate that oxygen moieties were consumed to form other interfacial bonds, which decreased the amount of Si-O, as previously discussed. In addition, we postulate that the silicon from the EVA side and nitrogen from the PET side formed bonds to generate more of a Si-N network. Note from the previous section that silicon from the EVA and nitrogen from the PET are present to promote stronger adhesion, and UV irradiation has facilitated the formation of new, additional bonds. Therefore, more Si-N bond formation and photopolymerization via consuming oxygen has led to an increase in interfacial adhesion strength for the $t_{1.5}$ samples.

For t_{24} samples, a higher O/C ratio of 0.34 was observed, and a decrease in adhesion strength. In this case, prolonged UV-induced oxidation proceeded, and it can be assumed that the photopolymerization ceased to develop as the competition between polymerization and oxidation processes has dominated to the latter process. In short, the prolonged UV-induced oxidation process proceeded, making the interface at the PET side more inert, resulting in facile delamination at the PET-EVA interface.

Another major difference among the samples was observed in the C 1s spectra, where a broad π-π* shake-up peak at 291.5 eV was detected in the t_{24} sample (**Figure 3.14**). The π-π* shake-up feature is a harbinger for aromatic systems [67]. This comes from the aromatic terephthalate group of the PET. As PET undergoes photodegradation, the UV light absorbing species such as ester carbonyl groups (Component D of C 1s spectra in **Table 3.4**) and aromatic phenyl rings are known to undergo photochemical degradation within the PET structure [68]. The data in **Table 3.4** also shows no signs of ester carbonyl groups, and the appearance of a π-π* shake-up peak demonstrates the photochemical degradation of the PET film, which affected the PET-EVA interface that led to a sharp

decrease in its interfacial adhesion strength (25% of the t_0 sample). In addition, the Si-O content was compared by deconvoluting the Si 2p peak (**Table 3.4**). While t_0 and $t_{1.5}$ samples contained 25.53 ± 2.52% and 13.48 ± 1.71% of Si-O, respectively, only 0.18 ± 0.20% was detected for the t_{24} samples. It is evident that UV exposure time has an inverse relationship with Si-O content; however, this phenomenon is not clearly understood and remains to be studied in future work.

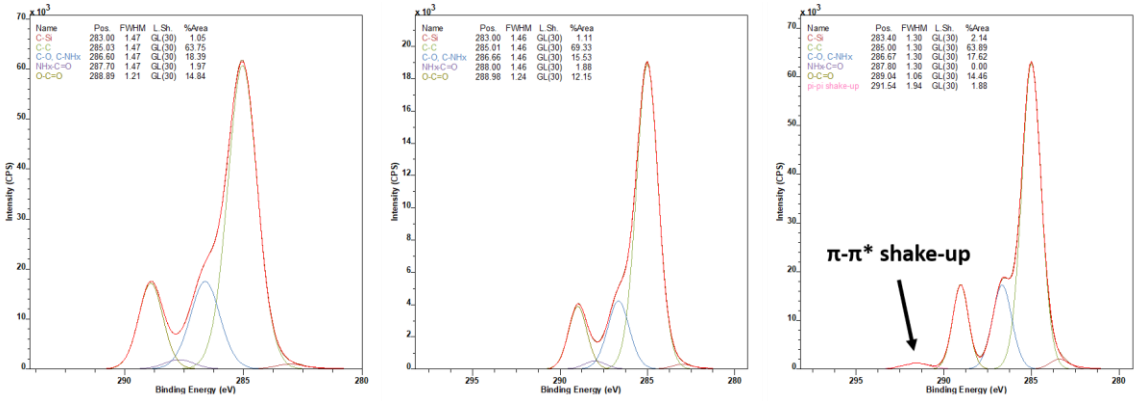

Figure 3.14 XPS C 1s spectra of (a) t_0 sample, (b) $t_{1.5}$ sample, and (c) t_{24} sample with π-π* shake-up peak at 291.5 eV.

Nonetheless, this section explores the effect of UV irradiation on the interfacial adhesion strength of the PET-EVA interface and attempts to investigate the interface chemistry to better understand the results of the adhesion test. During UV exposure, the surface temperature of the PET-EVA-PET encapsulation package was ~65 °C, which opens the possibility that both thermal and UV effects may have contributed to its degradation. Therefore, the next section discusses the effect of thermal aging at 65 °C on the adhesion properties of the same package design.

3.4.2 Effect of Thermal Aging on the PET-EVA Adhesion Chemistry

The interfacial adhesion strength between the PET and EVA of PET-EVA-PET sandwiched samples upon thermal aging at 65 °C is illustrated in **Figure 3.15** (in collaboration with M. Sulkis [56]). Initial peel strength decreases with thermal aging as the peel strength of $t_{1.5}$, t_3, and t_8 samples are well below that of the control sample, and as time of exposure progresses, a slight increase in peel strength was observed with t_{16}, t_{20}, and t_{24} samples. However, when accounting for the sample to sample variations, the thermal aging effect seems to be less significant than when UV aging was performed on the samples. Yet, XPS analysis on the selected samples is discussed in the next several paragraphs to evaluate any chemical changes on the interface to help interpret the mechanical characterization test results.

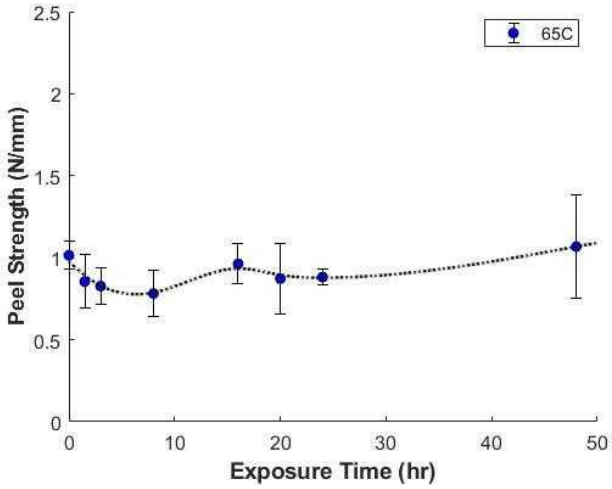

Figure 3.15 T-Peel test characterization of PET-EVA-PET interface upon thermal aging at 65 °C. In collaboration with M. Sulkis [56].

Table 3.5 summarizes the detected elemental peaks of delaminated PET surface upon thermal aging for 8 h, 16 h, and 24 h compared against the control sample without thermal aging. These data were calculated from the survey spectra and represents an average of 5 points on the surface. C 1s, O 1s, Si 2p, and N 1s peaks were detected in all samples. Noticeably, all thermally aged samples had higher O/C ratios, which demonstrates that thermal oxidation occurred.

Table 3.5 Average elemental composition from survey spectra of ST505 PET surfaces of delaminated T-Peel Samples upon thermal aging at 65 °C.

		t_0	t_8	t_{16}	t_{24}
Element (%)	C 1s	73.97 ± 0.92	68.96 ± 0.30	72.88 ± 0.62	73.53 ± 0.50
	O 1s	22.37 ± 0.95	24.61 ± 0.41	23.91 ± 0.68	23.66 ± 0.46
	Si 2p	1.31 ± 0.19	4.15 ± 0.31	0.71 ± 0.23	0.38 ± 0.18
	N 1s	2.35 ± 0.15	2.28 ± 0.24	2.51 ± 0.11	2.43 ± 0.11
O/C Ratio		0.30	0.36	0.33	0.32

As depicted in **Figure 3.16**, a set of t_8 samples has the highest O/C ratio and the lowest adhesion strength, a similar trend observed for a set of UV-aged t_{24} samples (**Figure 3.10** and **Table 3.3**). The reactions that occur at the surface of polymers, such as surface oxidation on the PET, EVA, or both, are complex. However, the surface oxidation of PET is reported to give a rise to a formation of terminal vinyl groups, phenols, and carboxylic acid end groups (COOH) [34, 69]. According to **Figure 3.17** (regenerated from the data in **Table 3.6**), a continuous decrease in C-C component, and increase in O-C=O component were observed, which are indicative of surface oxidation on the PET. Similar surface characteristics of PET was observed by the work of Gotoh et. al. [32].

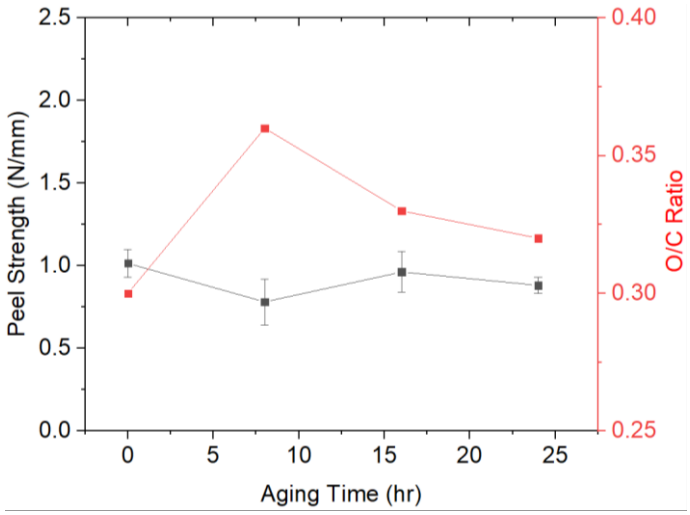

Figure 3.16 Peel strength values of the PET-EVA-PET interface and their O/C ratios upon thermal aging at 65 °C.

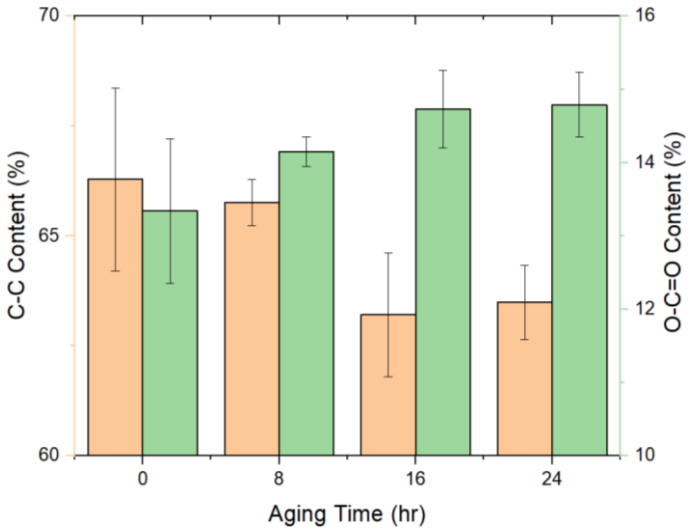

Figure 3.17 C-C and O-C=O component amounts for the delaminated PET-EVA samples upon thermal aging at 65 °C.

Table 3.6 Average binding energies and full width half maxima (FWHM) of C 1s, O 1s, and Si 2p spectra of ST505 PET surfaces of delaminated T-Peel samples upon thermal aging at 65 °C.

			Components	Binding Energy (eV)	FWHM	Area (%)
t_0	C 1s	A	C-Si	283.0 ± 0.1	1.48 ± 0.02	1.17 ± 0.05
		B	C-C, C-H	285.0 ± 0.1	1.48 ± 0.02	66.29 ± 2.08
		C	C-O, C-NH*x*	286.6 ± 0.1	1.48 ± 0.02	17.09 ± 1.23
		D	NH*x*-C=O	287.7 ± 0.1	1.48 ± 0.02	2.12 ± 0.15
		E	O-C=O	288.9 ± 0.1	1.23 ± 0.01	13.34 ± 0.98
	O 1s	A	NH*x*-C=O	530.2 ± 0.1	1.55 ± 0.01	2.25 ± 0.63
		B	O=C-O	532.1 ± 0.1	1.55 ± 0.01	55.62 ± 1.07
		C	O-C=O	533.6 ± 0.1	1.55 ± 0.01	42.13 ± 1.67
	Si 2p	A	Si-C	100.2 ± 0.2	1.74 ± 0.06	1.27 ± 0.34
		B	Si-N	101.8 ± 0.1	1.74 ± 0.06	26.10 ± 3.13
		C	N-Si-O	102.6 ± 0.1	1.74 ± 0.06	49.10 ± 1.81
		D	Si-O	103.5 ± 0.1	1.74 ± 0.06	25.53 ± 2.52
t_8	C 1s	A	C-Si	283.1 ± 0.1	1.55 ± 0.02	1.40 ± 0.11
		B	C-C, C-H	285.0 ± 0.1	1.55 ± 0.02	65.76 ± 0.53
		C	C-O, C-NH*x*	286.6 ± 0.1	1.55 ± 0.02	17.86 ± 0.25
		D	NH*x*-C=O	288.0 ± 0.1	1.55 ± 0.02	0.84 ± 0.20
		E	O-C=O	288.9 ± 0.1	1.26 ± 0.01	14.15 ± 0.20
	O 1s	A	NH*x*-C=O	530.0 ± 0.1	1.54 ± 0.01	1.54 ± 0.04
		B	O=C-O	532.0 ± 0.1	1.54 ± 0.01	61.26 ± 0.30
		C	O-C=O	533.5 ± 0.1	1.54 ± 0.01	37.19 ± 0.29
	Si 2p	A	Si-C	99.6 ± 0.1	1.75 ± 0.06	1.22 ± 0.11
		B	Si-N	101.9 ± 0.1	1.75 ± 0.06	53.93 ± 1.66
		C	N-Si-O	102.7 ± 0.1	1.75 ± 0.06	43.04 ± 1.37
		D	Si-O	104.3 ± 0.2	1.75 ± 0.06	1.81 ± 0.34
t_{16}	C 1s	A	C-Si	283.0 ± 0.1	1.48 ± 0.03	1.20 ± 0.05
		B	C-C, C-H	285.0 ± 0.1	1.48 ± 0.03	63.21 ± 1.41
		C	C-O, C-NH*x*	286.6 ± 0.1	1.48 ± 0.03	18.51 ± 0.77
		D	NH*x*-C=O	287.8 ± 0.1	1.48 ± 0.03	2.35 ± 0.37
		E	O-C=O	288.9 ± 0.1	1.23 ± 0.02	14.73 ± 0.53
	O 1s	A	NH*x*-C=O	530.3 ± 0.2	1.53 ± 0.03	2.36 ± 0.59
		B	O=C-O	531.9 ± 0.1	1.53 ± 0.03	52.97 ± 0.93
		C	O-C=O	533.4 ± 0.1	1.53 ± 0.03	44.67 ± 0.55
	Si 2p	A	Si-C	100.0 ± 0.3	1.89 ± 0.09	2.36 ± 1.10
		B	Si-N	101.8 ± 0.1	1.89 ± 0.09	34.79 ± 1.31
		C	N-Si-O	103.2 ± 0.1	1.89 ± 0.09	55.82 ± 2.65
		D	Si-O	104.2 ± 0.2	1.89 ± 0.09	7.02 ± 3.83
t_{24}	C 1s	A	C-Si	283.0 ± 0.1	1.46 ± 0.01	1.17 ± 0.03
		B	C-C, C-H	285.0 ± 0.1	1.46 ± 0.01	63.49 ± 0.84
		C	C-O, C-NH*x*	286.6 ± 0.1	1.46 ± 0.01	18.61 ± 0.43
		D	NH*x*-C=O	287.8 ± 0.1	1.46 ± 0.01	1.94 ± 0.11
		E	O-C=O	288.8 ± 0.1	1.19 ± 0.01	14.79 ± 0.44
	O 1s	A	NH*x*-C=O	530.1 ± 0.1	1.50 ± 0.01	1.80 ± 0.06
		B	O=C-O	531.9 ± 0.1	1.50 ± 0.01	52.91 ± 0.21
		C	O-C=O	533.4 ± 0.1	1.50 ± 0.01	45.28 ± 0.24
	Si 2p	A	Si-C	99.9 ± 0.1	2.38 ± 0.11	1.59 ± 1.40
		B	Si-N	102.0 ± 0.2	2.38 ± 0.11	14.12 ± 8.26
		C	N-Si-O	102.9 ± 0.2	2.38 ± 0.11	78.95 ± 9.30
		D	Si-O	104.1 ± 0.2	2.38 ± 0.11	5.33 ± 2.11

In addition, a sharp increase of silicon content was observed for a set of t_8 samples (**Table 3.5** and **Figure 3.18**); however, the origin of the increase in silicon content cannot be convulsively drawn from the limited data. A decrease in Si-O content by ~5-fold was observed for all sets of t_8, t_{16}, and t_{24} samples (**Figure 3.18**). The decrease in Si-O content is countered by the presence of a relatively higher amount of Si-N and N-Si-O bonds for the thermally-aged samples (**Figure 3.19**). From the deconvolution of Si 2p spectra, it is clearly seen that Si-N and N-Si-O bonds are dominant over Si-C and Si-O bonds. This could either suggest that (1) Si-C or Si-O bonds were broken while delamination occurred or (2) thermal aging provided more Si-N and N-Si-O bond formations. However, as stated previously, there is no evidence that either thermal or UV aging decreases the Si-O content, while increasing the Si-N or N-Si-O contents. **Figure 3.19** and **Table 3.6** indicate the increase in FWHM for thermally-aged samples (broader component peaks), from 1.74 ± 0.06 (t_0) to 1.89 ± 0.09 (t_{16}) and 2.38 ± 0.11 (t_{24}) and the binding energy shift of Si-O component from 103.5 ± 0.1 eV (t_0) to a higher peak position of 104.3 ± 0.2 eV (t_8), 104.2 ± 0.2 eV (t_{16}), and 104.1 ± 0.2 eV (t_{24}). In this case, it is probable that other species are present for t_{16} and t_{24} samples that contribute to the apparent broadening. Also, the shift in the maxima of silicon oxide peaks towards a higher binding energy reflects the increase in relative moieties of higher oxidative states [70]. Nonetheless, understanding the changes in the FWHM values and binding energy shifts is a topic for future work.

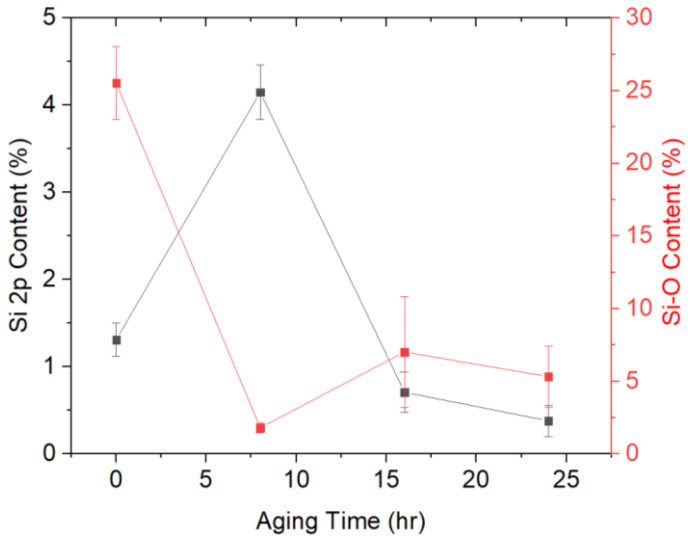

Figure 3.18 Si 2p content and Si-O content of the delaminated PET-EVA samples upon thermal aging at 65 °C.

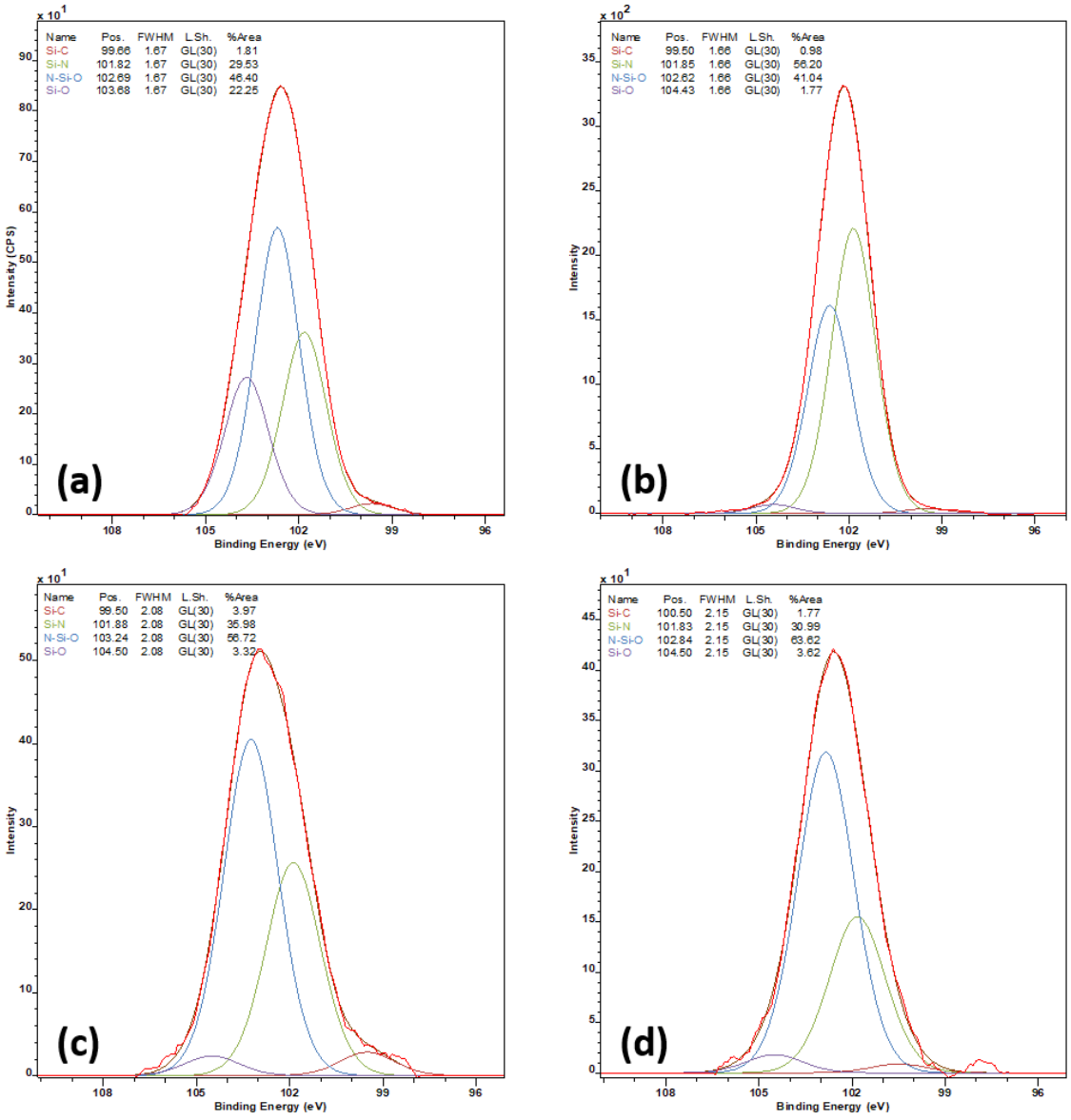

Figure 3.19 XPS Si 2p spectra of (a) t_0 sample, (b) t_8 sample, (c) t_{16} sample, and (d) t_{24} sample upon thermal aging at 65 °C.

From this section, the effect of thermal-aging on the oxidation of the PET-EVA samples was discussed and was not found to be correlated with adhesion strength. The next section discusses the effect of thermal-aging on the adhesion behavior and its chemistry upon damp-heat aging on the same PET-EVA-PET test specimens.

3.4.3 Effect of Damp-Heat Aging on the PET-EVA Adhesion Chemistry

The interfacial adhesion strength between the PET and EVA of PET-EVA-PET sandwiched samples upon damp-heat aging at 85 °C/85% R.H is illustrated in **Figure 3.20** (in collaboration with M. Sulkis [56]). The peel strengths of the samples increased with increased exposure to damp-heat aging until 16 h of damp-heat exposure and plateaus out from there. A similar adhesion trend on a longer time scale was observed from a test conducted by NREL [55], which is depicted in **Figure 3.21**. Although their architecture is slightly different from the one used in this study, the adhesion failure will primarily occur at the PET-EVA interface before delaminating at the Glass-EVA interface due to the presence of a strong Si-O-Si inorganic network. Although the peel strength trends upon damp-heat exposure are well studied, the mechanistic study involving chemical analysis of the delaminated surface is lacking. Therefore, the samples were analyzed with XPS and the results are discussed in the next several paragraphs to evaluate any chemical changes on the interface to help interpret the mechanical characterization test results.

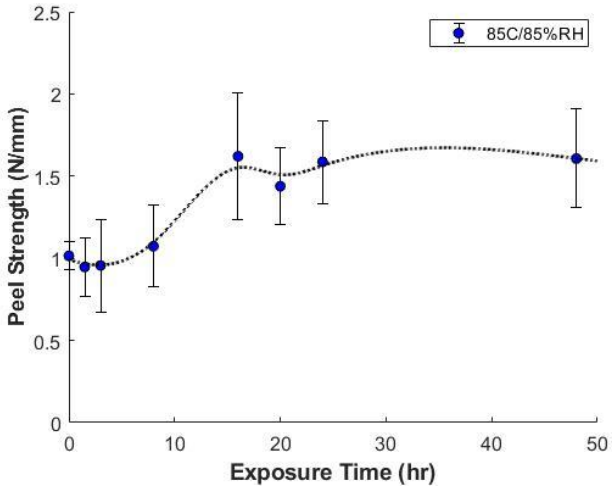

Figure 3.20 T-Peel test characterization of PET-EVA-PET interface upon 85 °C/85% R.H. damp-heat aging. In collaboration with M. Sulkis [56].

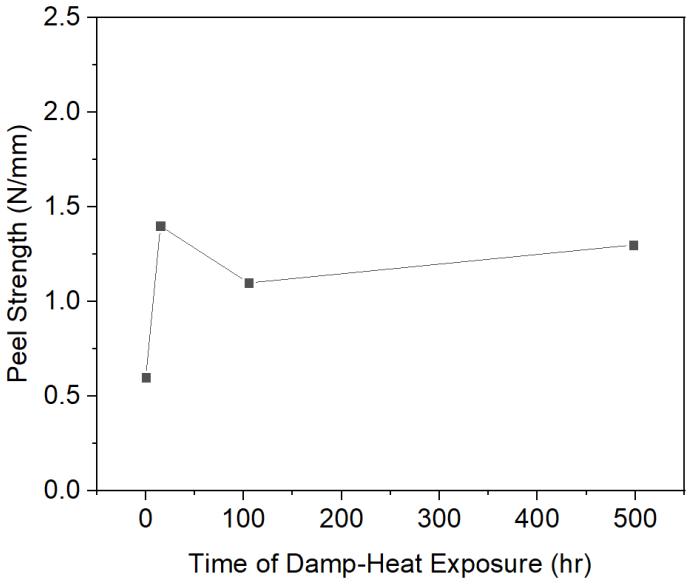

Figure 3.21 Adhesion strength of PET-EVA-Glass construction upon 85 °C/85% R.H. damp-heat exposure by NREL. Adapted from reference [55].

Table 3.7 summarizes the detected elemental peaks of delaminated PET surface upon damp-heat exposure for 1.5 h, 16 h, and 24 h compared against the control sample without thermal aging. These data were calculated from the survey spectra and represents an average of 5 points on the surface. C 1s, O 1s, Si 2p, and N 1s peaks were detected in all samples. Noticeably, all samples with damp-heat exposure have lower O/C ratios, which demonstrates that chemical reactions involving the consumption of oxygen moieties may have occurred. This was not the case for the UV and thermally exposed samples discussed earlier.

Table 3.7 Average elemental composition from survey spectra of ST505 PET surfaces of delaminated T-Peel samples upon 85 °C/85% R.H. damp-heat aging.

		t_0	$t_{1.5}$	t_{16}	t_{24}
Element (%)	C 1s	73.97 ± 0.92	75.70 ± 0.32	75.25 ± 0.45	75.23 ± 0.42
	O 1s	22.37 ± 0.95	20.36 ± 0.14	21.49 ± 0.33	22.25 ± 0.16
	Si 2p	1.31 ± 0.19	1.62 ± 0.51	0.60 ± 0.05	0.28 ± 0.16
	N 1s	2.35 ± 0.15	2.32 ± 0.15	2.67 ± 0.17	2.24 ± 0.21
O/C Ratio		0.30	0.27	0.29	0.30

Upon the lamination process between the PET and EVA, silane coupling agents from EVA are bonded to the hydroxyl (–OH) and amine (–NH2) groups. This newly formed interface is depicted in **Figure 3.22a**. However, upon the damp-heat exposure, the alkoxy groups undergo a hydrolysis reaction at the interface to form hydroxy groups, which can be described as:

$$\text{PET-O-Si-}(OCH_3)_2\text{-R'-O-EVA} \rightleftharpoons \text{PET-O-Si-}(OH)_2\text{-R'-O-EVA} \quad (3.1)$$

This hydrolysis reaction in equation (3.1) takes place to form a silanol group in the presence of water, which is available from the moisture from the environmental chamber. In addition, a condensation reaction occurs to form a siloxane (Si-O-Si) linkage, but there is also a reverse hydrolysis reaction, i.e. condensation, at the surface. This surface equilibrium reaction can be described as shown in equation (3.2) [57]:

$$HO\text{-}Si\text{-}OH + HO\text{-}Si\text{-}OH \rightleftharpoons H_2O + Si\text{-}O\text{-}Si \qquad (3.2)$$

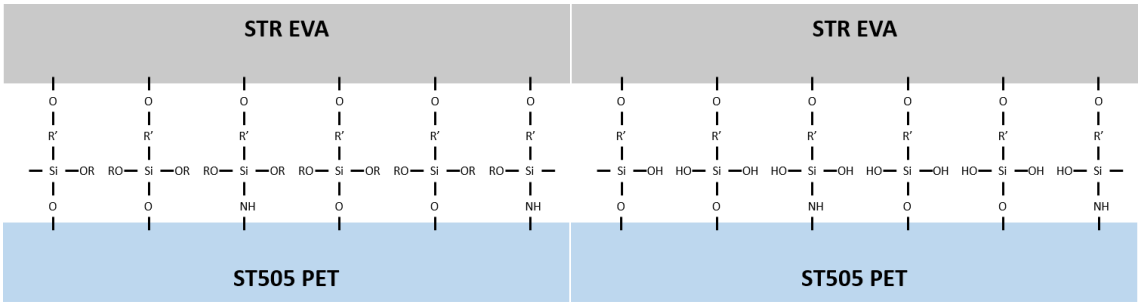

(a) (b)

Figure 3.22 Schematic of PET-EVA interface (a) upon lamination process and (b) upon damp-heat exposure. Note that –OR represents –(OCH_3) and –R'– represents –$CH_2CH(CH_3)CO_2(CH_2)_3$)– groups.

Therefore, during damp-heat exposure, it can be hypothesized that the concentration of siloxane linkages has increased (**Figure 3.22b**). This can be supported by **Figure 3.23**. While samples exposed to UV and thermal heat for 24 h, when delaminated resulted in only 0.18 ± 0.20% and 5.33 ± 2.11% of Si-O content, respectively, samples with damp-heat exposure resulted in much greater 20.58 ± 6.80% of Si-O content. In addition, the concentration of Si-O increased as the damp-heat exposure time increased in **Table 3.8**: 17.94 ± 4.13%, 18.02 ± 6.48%, and 20.58 ± 6.80%, respectively for $t_{1.5}$, t_{16}, and t_{24} samples. Although the Si-O content is lower than in the t_0 samples, 25.53 ± 2.52 %, from equation

(3.2) and **Figure 3.22,** the amount of oxygen decreases as condensation reactions lead to the formation of Si-O-Si linkages. This is also supported from the decrease in O/C ratio, reported in **Table 3.7,** that the once present methoxy groups were hydrolyzed upon damp-heat exposure. Therefore, the increase in adhesion strength shown in **Figure 3.20**, can be explained due to the formation of a strong Si-O-Si network present in the damp-heat exposed samples.

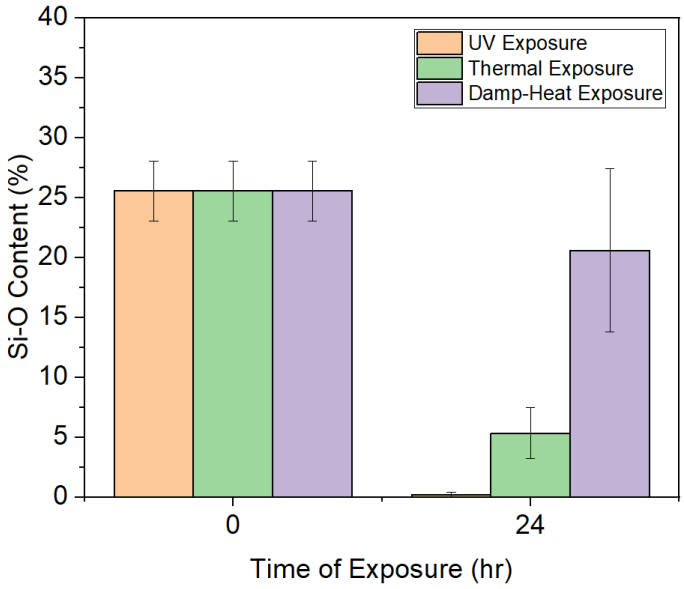

Figure 3.23 Si-O content change after 24 hr of exposure to UV at 365 nm, thermal at 65 °C, and damp-heat at 85 °C/85% R.H.

Table 3.8 Average binding energies and full width half maxima (FWHM) of C 1s, O 1s, and Si 2p spectra of ST505 PET surfaces of delaminated T-Peel samples upon 85 °C/85% R.H. Aging.

			Components	Binding Energy (eV)	FWHM	Area (%)
t_0	C 1s	**A**	C-Si	283.0 ± 0.1	1.48 ± 0.02	1.17 ± 0.05
		B	C-C, C-H	285.0 ± 0.1	1.48 ± 0.02	66.29 ± 2.08
		C	C-O, C-NH*x*	286.6 ± 0.1	1.48 ± 0.02	17.09 ± 1.23
		D	NH*x*-C=O	287.7 ± 0.1	1.48 ± 0.02	2.12 ± 0.15
		E	O-C=O	288.9 ± 0.1	1.23 ± 0.01	13.34 ± 0.98
	O 1s	**A**	NH*x*-C=O	530.2 ± 0.1	1.55 ± 0.01	2.25 ± 0.63
		B	O=C-O	532.1 ± 0.1	1.55 ± 0.01	55.62 ± 1.07
		C	O-C=O	533.6 ± 0.1	1.55 ± 0.01	42.13 ± 1.67
	Si 2p	**A**	Si-C	100.2 ± 0.2	1.74 ± 0.06	1.27 ± 0.34
		B	Si-N	101.8 ± 0.1	1.74 ± 0.06	26.10 ± 3.13
		C	N-Si-O	102.6 ± 0.1	1.74 ± 0.06	49.10 ± 1.81
		D	Si-O	103.5 ± 0.1	1.74 ± 0.06	25.53 ± 2.52
$t_{1.5}$	C 1s	**A**	C-Si	283.2 ± 0.1	1.41 ± 0.01	1.21 ± 0.14
		B	C-C, C-H	285.0 ± 0.1	1.41 ± 0.01	69.67 ± 1.44
		C	C-O, C-NH*x*	286.6 ± 0.1	1.41 ± 0.01	14.57 ± 0.99
		D	NH*x*-C=O	287.5 ± 0.1	1.41 ± 0.01	2.59 ± 0.17
		E	O-C=O	289.0 ± 0.1	1.23 ± 0.01	11.96 ± 0.62
	O 1s	**A**	NH*x*-C=O	530.1 ± 0.1	1.56 ± 0.01	1.20 ± 0.06
		B	O=C-O	532.0 ± 0.1	1.56 ± 0.01	52.59 ± 0.44
		C	O-C=O	533.5 ± 0.1	1.56 ± 0.01	46.21 ± 0.50
	Si 2p	**A**	Si-C	99.8 ± 0.2	1.97 ± 0.08	0.49 ± 0.22
		B	Si-N	101.6 ± 0.1	1.97 ± 0.08	33.24 ± 4.07
		C	N-Si-O	102.8 ± 0.1	1.97 ± 0.08	48.33 ± 1.24
		D	Si-O	103.9 ± 0.1	1.97 ± 0.08	17.94 ± 4.13
t_{16}	C 1s	**A**	C-Si	283.0 ± 0.1	1.45 ± 0.01	1.09 ± 0.03
		B	C-C, C-H	285.0 ± 0.1	1.45 ± 0.01	66.23 ± 0.58
		C	C-O, C-NH*x*	286.5 ± 0.1	1.45 ± 0.01	16.25 ± 0.29
		D	NH*x*-C=O	287.5 ± 0.1	1.45 ± 0.01	2.71 ± 0.25
		E	O-C=O	288.9 ± 0.1	1.25 ± 0.01	13.72 ± 0.31
	O 1s	**A**	NH*x*-C=O	530.1 ± 0.1	1.53 ± 0.01	1.54 ± 0.12
		B	O=C-O	532.0 ± 0.1	1.53 ± 0.01	53.15 ± 0.15
		C	O-C=O	533.5 ± 0.1	1.53 ± 0.01	45.32 ± 0.18
	Si 2p	**A**	Si-C	100.2 ± 0.1	2.23 ± 0.16	0.05 ± 0.04
		B	Si-N	101.7 ± 0.2	2.23 ± 0.16	31.31 ± 3.79
		C	N-Si-O	103.0 ± 0.2	2.23 ± 0.16	50.62 ± 4.38
		D	Si-O	103.8 ± 0.1	2.23 ± 0.16	18.02 ± 6.48
t_{24}	C 1s	**A**	C-Si	283.0 ± 0.1	1.45 ± 0.01	1.15 ± 0.01
		B	C-C, C-H	285.0 ± 0.1	1.45 ± 0.01	65.58 ± 0.24
		C	C-O, C-NH*x*	286.6 ± 0.1	1.45 ± 0.01	17.10 ± 0.23
		D	NH*x*-C=O	287.7 ± 0.1	1.45 ± 0.01	2.20 ± 0.12
		E	O-C=O	288.9 ± 0.1	1.23 ± 0.01	13.97 ± 0.21
	O 1s	**A**	NH*x*-C=O	530.1 ± 0.1	1.52 ± 0.01	1.43 ± 0.04
		B	O=C-O	532.0 ± 0.1	1.52 ± 0.01	52.74 ± 0.14
		C	O-C=O	533.5 ± 0.1	1.52 ± 0.01	45.83 ± 0.11
	Si 2p	**A**	Si-C	100.2 ± 0.2	2.21 ± 0.14	0.70 ± 0.32
		B	Si-N	102.0 ± 0.2	2.21 ± 0.14	33.97 ± 5.86
		C	N-Si-O	103.1 ± 0.2	2.21 ± 0.14	44.75 ± 7.03
		D	Si-O	104.0 ± 0.2	2.21 ± 0.14	20.58 ± 6.80

3.5 Summary

This chapter explored UV, thermal, and damp-heat degradation on the PET-EVA-PET encapsulated samples. T-Peel mechanical characterization yielded adhesion strength and XPS surface characterization yielded surface chemical components upon individual aging condition. It was understood that some degree of aging, for example ~3 h of UV exposure to the sample, enhance the adhesion; however, a longer exposure to the samples are necessary to understand the holistic behaviors on adhesion and surface chemistry. Understanding the interface and adhesion chemistry is extremely difficult. However, this study and analysis provide an insight into the possible degradation pathway only inferred from our experimental data and supporting literature reviews.

CHAPTER 4. CONCLUSION

4.1 Summary and Conclusion

The research in this dissertation has been conducted to investigate degradation behavior of the PET backsheet and PV encapsulant interface upon UV, thermal, and damp-heat aging tests. Since the PSCs are highly susceptible to degradation from adverse environments, resolving the issue of these reliability of the PSC modules are of primary challenge. However, this issue can be mitigated and be suppressed by improving the adhesion strength between the PET backsheet and PV encapsulant. Several attempts have been explored throughout the dissertation:

- Chapter 2 investigated the thermal and moisture stability of PDMS-based adhesive bonded to the surface-modified polymer backsheets using coupling agents and physical treatments for PSC module packaging applications. Surface modification on the PET backsheet was done chemically by organic silane-based coupling agents and physically by UV/Ozone treatment. Although significant increase in adhesion strengths were reported initially before any aging conditions, those values significantly dropped upon the thermal and moisture aging tests. Thus, different surface modification technique will be required to maintain the adhesion strength hence the damp-heat stability of these modules via PECVD-assisted deposition of inorganic molecules.
- Chapter 3 investigated the UV, thermal, and damp-heat stability of thermally-curable EVA adhesive bonded to the PET backsheet. This chapter addressed

the degradation of the interface by monitoring the adhesion strength upon UV, thermal, and damp-heat exposure. In addition, interface chemistry of the delaminated samples upon individual aging condition was investigated. However, a similar test but on a longer time scale is necessary to observe the long-term effect of aging on these samples.

Overall, degradation mechanism has been studied through the dissertation, which are of greatest importance to ensure stability of the PSC modules in the future. From these findings, continuous efforts on the development to suppress moisture ingress through the interfaces of the encapsulated modules and on the understanding of the premature-failure under the exposure of different environmental conditions should be made. To this end, recommendations for future work are presented.

4.2 Recommendations for Future Work

4.2.1 Background

Up to now, PSCs can only last up to 6 months at an outdoor environment because they are susceptible to harsh environmental conditions such as extreme amount of UV rays, temperature, and high humidity. Currently a glass-to-glass encapsulation method has been used for the 1st and 2nd generation encapsulation of PSCs, where glass slides serve as both frontsheet and backsheet, and getter-filled PIB and PDMS are used as the edge seal and encapsulant respectively [16]. This type of structure, utilizing PIB as an edge seal, is required to protect the PSCs from adverse environmental conditions, especially from moisture. PIB is known for having one of the lowest water vapor transmission rates (WVTR) reportedly 0.01 to 0.001 gm^{-2} day^{-1} [17], whereas a most common PDMS

elastomer (Sylgard 184), is ~900 gm^{-2} day^{-1} [18]. It is also reported that a 1.25 cm wide getter-filled PIB edge seal as a moisture barrier can pass IEC 61646 (1000 h at 85 °C/85% R.H.), which is equivalent to a 25-year lifetime at an outdoor environment [19].

However, for the next generation encapsulation method it would be valuable to minimize or eliminate the need for an opaque edge sealant. This will increase the available area for light-harvesting regions of PSCs and will simplify the encapsulation process, presumably aiding high-volume manufacturing as it removes an additional lamination step. It is also crucial that frontsheets and backsheets be replaced by transparent and flexible polymer barrier films for the next generation encapsulation method to be compatible with roll-to-roll processing. This would provide for fast, efficient, and large-scale processing of flexible thin film solar cells [20]. We propose to design a novel transparent polymer blend of PIB and PDMS as an encapsulant (adhesive) material for PV module packaging. Previously mentioned in **Figure 1.2** illustrates the difference between the conventionally used encapsulation method for PSC package and our proposed method. Therefore, we propose enhanced moisture transport properties and interfacial adhesion strength of our transparent polymer blends compared to commercially available PDMS-based adhesives for PV module packaging applications.

The designed transparent adhesive in this study was a mixture of thermoplastic transparent pure butyl rubber (PIB) without any fillers and thermally-cured thermoset PDMS-based adhesive with UV absorber and UV stabilizer fillers for PV applications. In this study, we characterized the moisture ingress and performed interfacial adhesion strength through designed transparent polymer blends of different mixing ratios via optical calcium measurement tests and T-Peel tests, respectively. The moisture ingress results were

compared to the commercially available PIB edge seal and PDMS-based adhesive to benchmark our data. This study serves to provide an improvement in packaging materials and in encapsulation processes with the introduction of a new type of adhesive composite.

4.2.2 Experimental Section

A transparent, two part-addition cure PDMS adhesive and a transparent thermoplastic PIB melt (45,000 $gmol^{-1}$) were used as encapsulants. Multilayer barrier films with a PET carrier were used as a transparent and flexible polymer frontsheet and backsheet for T-Peel test coupons. Optical calcium samples were deposited on a borosilicate glass and a cover glass was used as a frontsheet for optical calcium test coupons.

PDMS and PIB stock solutions were prepared by mixing part A of PDMS adhesive and PIB melt, respectively, with toluene solvent into 1:2 ratio by weight. The individual stock solutions were mixed thoroughly using a magnetic stirrer for overnight to fully dissolve the polymer into the solvent at 80 °C and at 1600 rpm. PDMS and PIB blends were mixed into separate glass vials in 3 ratios by weight as shown in **Table 4.1**. Note that these ratios in **Table 4.1** are respective to PDMS:PIB. These polymer blends were also mixed thoroughly using the same stirring conditions. Note that part B (cross-linking agent with catalyst) of PDMS adhesive was added to the polymer blend solution according to the manufacturer's specification before utilizing the solution for fabricating either optical calcium test coupons or T-Peel test coupons.

Table 4.1 PDMS and PIB blend ratios.

PDMS Stock Solution	Blend A	Blend B	Blend C	PIB Stock Solution
1:0	3:1	1:1	1:3	0:1

The polymer blend was spin-coated onto the cover glass at room temperature at 500 rpm for 60 s to ensure full coverage of polymer blend solution on the cover glass and 1500 rpm for another 60 seconds to ensure uniform thickness of the polymer blend and to remove residual toluene solvent. During each spin-coating step, 1 mL of polymer solution was dropped onto the cover glass before initiation.

The cover glass was bonded with the calcium coated borosilicate glass using a press with an applied force of 65 psi, and the bonded test coupon was cured at 100 °C for 1 h (manufacture's specification for PDMS). **Figure 4.1** illustrates a representative schematic of as-prepared test coupon for optical calcium screening test. Note from **Figure 4.1b** that our formulated barrier adhesive (encapsulant) is optically transparent as both the gray calcium on glass and Texwipe are visible.

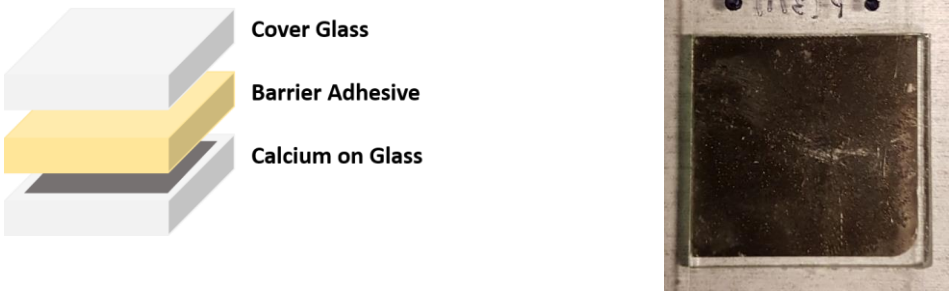

(a) (b)

Figure 4.1 (a) Schematic layer-by-layer structure of an optical calcium test coupon and (b) Top-view of the fabricated optical calcium test coupon.

Calcium test coupons were then put into the environmental chamber set at 85 °C/85% R.H., and these samples were scanned periodically to quantitatively calculate the effective moisture ingress. How optical calcium sample screening test could be utilized to deduce moisture ingress through the sample can be explained using equation (4.1). In this equation, calcium before reacting with water is optically opaque at visible light; however, upon reacting with moisture, calcium corrodes into calcium (II) hydroxide, which is optically transparent at visible light. As the samples were periodically scanned, calculating the effective area loss would be used to extrinsically calculate for moisture ingress values.

$$Ca_{(s)} + 2H_2O \rightleftharpoons Ca(OH)_{2\,(aq)} + H_{2\,(g)} \qquad (4.1)$$

A Universal Testing Machine (Test Resources, Shakopee, MN) was used to perform displacement-controlled T-peel experiments at 100 mm/minute. The same test condition and set-up were used from Chapter 2 (refer to **Figure 2.4**) and the same test coupon architecture was used from Chapter 3 (refer to **Figure 3.2**). Note that PDMS:PIB blends were used as an encapsulant material instead of the EVA sheets.

Thermogravimetric analysis (TGA) and differential scanning calorimetry (DSC) characterizations were performed. A TGA Q5000 (TA Instruments, New Castle, DE) was used to perform TGA characterization tests for all polymer samples. Temperature was reached from 25 °C to 800 °C with a ramping rate of 20 °C/min. Weight change was calculated using the software. A DSC Q2000 (TA Instruments, New Castle, DE) equipped with a cooling system was used to perform DSC characterization test for all polymer samples. Temperature was reached from -80 °C to 0 °C with a ramping rate of 10 °C/min. Glass transition temperature (T_g) was obtained using the software.

4.2.3 Morphology of Barrier Adhesives (PDMS:PIB Blend)

The morphology of polymer blends of PDMS and PIB were characterized using optical microscope. **Figure 4.2** compares different morphologies across different polymer blends used in this study. In **Figure 4.2a**, a typical sea-island type second phase of PIB is observed in PDMS matrix (Blend A). This morphology is also observed from the study Peng and his co-workers [71]. When added more PIB into the PDMS matrix (Blend B with 1:1 ratio), the second phase of PIB coalesced into a larger size (**Figure 4.2b**). Finally, this coalescence reached the saturation point and the phase inversion was occurred (**Figure 4.2c**). Therefore, when more PIB concentration was increased, the aspect ratio of PIB in the PDMS matrix increased and lost the droplet structure. Also note that the scale bar for **Figure 4.2a** is much smaller than that for **Figure 4.2b** and **Figure 4.2c**. It is hypothesized from this morphology that Blend A would have the lowest moisture ingress as the smaller and more uniformly confined droplet structure of PIB is well dispersed within the PDMS matrix that will suppress facile-ingress of moisture through this complex.

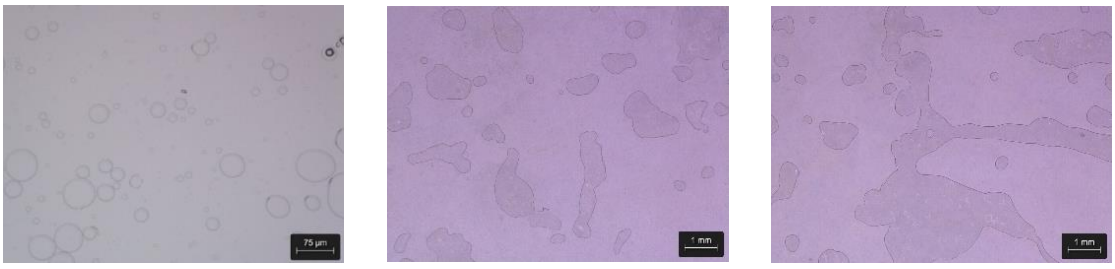

(a) (b) (c)

Figure 4.2 Optical microscope images showing the morphologies of (a) Blend A, (b) Blend B, and (c) Blend C.

4.2.4 Moisture Ingress Through Barrier Adhesives

The moisture ingress values (K values) were obtained after processing the calcium corrosion test. In **Figure 4.3a**, ingress distance of the three polymer blends is plotted against exposure time under the damp heat environment (85 °C/85% R.H.). Also, they were compared to a commercially available encapsulants for PV module packaging applications. The K values are plotted in **Figure 4.3b** using the information from **Figure 4.3a**. Results indicate that our polymer blends have K values in between the two commercially available products. Note that the previously mentioned getter-filled PIB that can sustain a 25-year lifetime at an outdoor environment have K value of 0.013, a magnitude lower than the polymer blend that has the lowest K value of 0.23 (Blend A). It was previously hypothesized that Blend A would have the lowest moisture ingress through the calcium coupons from the morphology analysis. Although the blends with higher concentration of moisture-blocking PIB were added into the PDMS matrix, due to the phase inversion and high-aspect ratio PIB morphology, higher K values were obtained for Blend B (0.50) and Blend C (0.26).

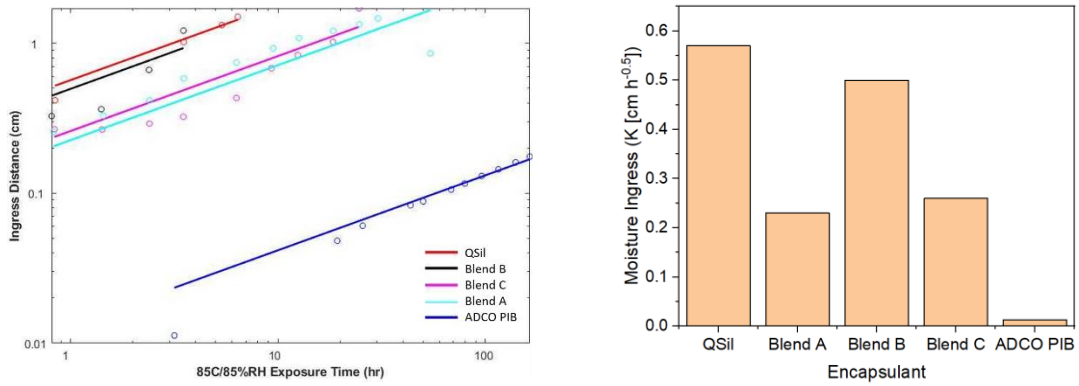

(a) (b)

Figure 4.3 (a) Moisture permeation through polymer blends via calcium corrosion testing at 85 °C/85% R.H. and (b) their calculated K values. In collaboration with M. Sulkis [56].

4.2.5 Adhesion Strength between Barrier Adhesives and PET Carrier Films

Adhesion strength between the PET (lamination side of the barrier film) and the barrier adhesive is one of the crucial factors that affects moisture ingress through the interfaces [35, 72]. Stronger the adhesion, more reliable bonds are formed at the interface due to the stronger network generated between the functional groups present from each layer. In **Figure 4.4** and **Figure 4.5**, adhesion strength between two polymeric materials used in this study (PDMS and PIB) and polymer surface (PET) were evaluated using T-Peel test method. Note that PIB-PET has a much stronger adhesion strength (0.57 N/cm) than that of PDMS-PET (0.22 N/cm). Delamination profile (**Figure 4.4**) shows that PDMS delaminates much more uniformly and cleanly while PIB delaminates in random fashion, but for sure, more energy is required to de-bond PIB from a PET carrier. Although **Figure 4.4** does not define a specific delamination pattern, it can provide an information that there are relatively weaker regions at the interface (**Figure 4.4b**). This explanation could also

suggest why moisture ingress was not uniform throughout as some regions with stronger interface would require more time for the moisture to ingress through the blends that contained PIB. Furthermore, lower adhesion strength values have higher susceptibility for delamination, which can reduce the moisture barrier efficiency and corrosion of metals [73, 74]. Therefore, the stronger interface formed for PIB-PET samples could explain for slower moisture ingress (delaying calcium corrosion) observed in **Figure 4.3** for the polymer blends and pure PIB polymer.

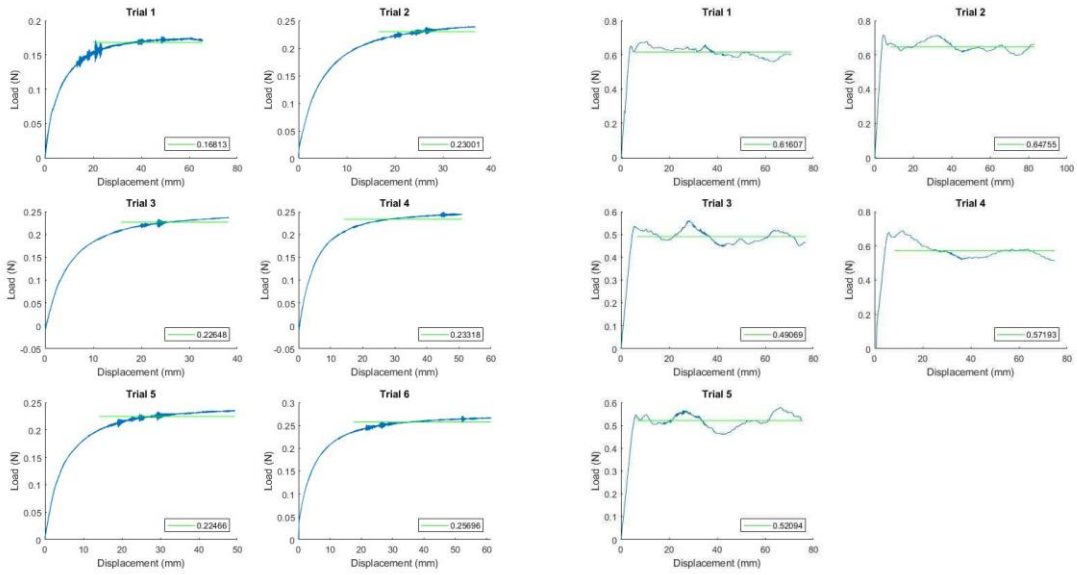

(a) (b)

Figure 4.4 T-Peel test data of (a) PDMS samples and (b) PIB samples. In collaboration with M. Sulkis [56].

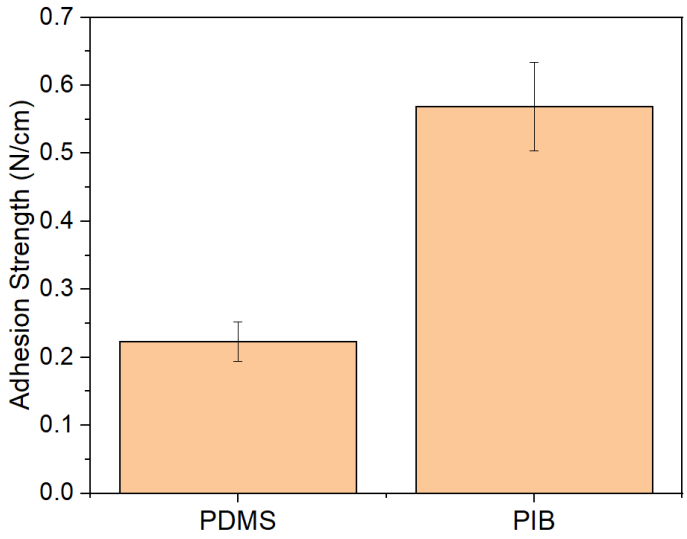

Figure 4.5 Calculated adhesion strength of PDMS-PET and PIB-PET.

4.2.6 Barrier Adhesive Characterizations

Polymer blends synthesized in this study were also characterized using TGA and DSC analysis to understand their thermal profiles and thermal stabilities for PV encapsulant applications. From **Figure 4.6a**, the pyrolysis temperature of PIB is much lower than that of PDMS. The TGA plot of the PDMS-PIB blend has two on-set decomposition temperatures: the earlier being that of PIB and the latter being that of the PDMS. Therefore, it is supported from this TGA plot that polymer blend was not mixed at the molecular level and was rathe mixed physically. In another words, the synthesized PDMS-PIB blend has a phase separation, which was observed earlier from the sea-island structure in **Figure 4.2**. The remaining weight from PDMS-PIB blend and pure PDMS is the O-Si-O backbone from the PDMS.

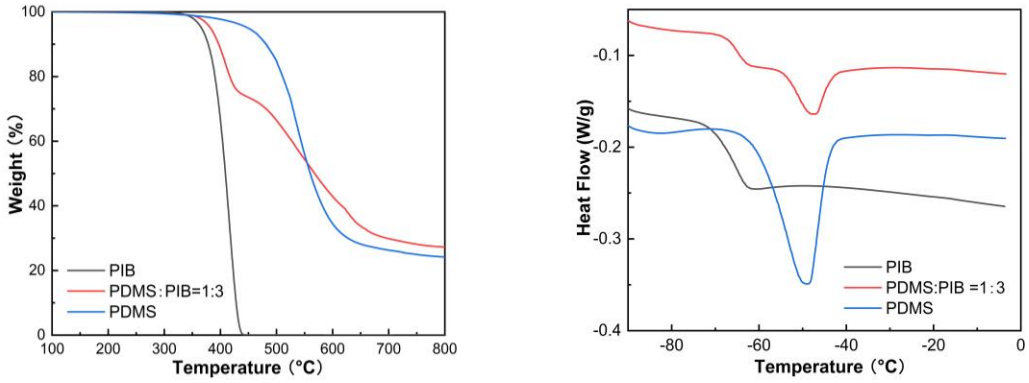

(a) (b)

Figure 4.6 Characterization plots of polymer blends using (a) TGA and (b) DSC.

From **Figure 4.6b** PDMS-PIB blend is shown with an endothermic peak known as the melting temperature (T_m), as well as the glass transition temperature (T_g). The endothermic peak of PDMS is attributed to the melts of the solid phase that was formed from devitrification and cold crystallization, which is typically observed in rubber materials; however, the mechanism has not been clearly understood yet. It was obtained from thermal analysis that T_g for the pure PIB is -65.29 °C, and that of this blend (Blend C) is slightly higher -66.07 °C. Because a typical T_g of PDMS is around -125 °C, it was not observed from our DSC analysis. In addition, T_m increases when PIB was added to PDMS as the endothermic peaks are shifted to the right. The DSC curve also suggests that the polymer blend was not mixed at the molecular level. It is suggested that in order to mix them at the molecular level, homogenizing agents must be used. In short, the polymer blends are well-suited as the encapsulants for thin-film PV applications because they are stable at temperature greater than 200 °C, and they are also flexible at room temp as the T_g for all samples were much below sub-zero temperature (less than -60 °C).

4.2.7 Hardness of the Barrier Adhesive

Mechanical testing of the polymer blends was conducted using the hardness testing method. From **Figure 4.7**, hardness of the polymer decreases with increased PIB content. Note that hardness value of pure PIB was unmeasurable due to a highly viscous character at room temperature.

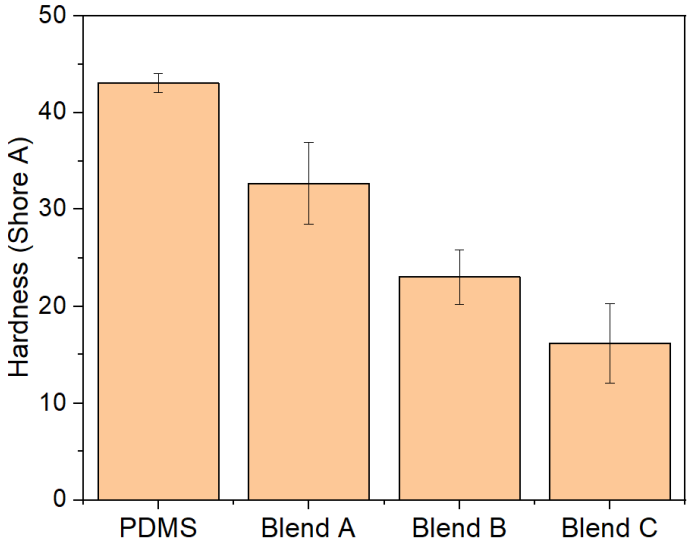

Figure 4.7 Harness test data of polymer blends.

Because the thermoset PDMS polymer is crosslinked, it is expected to have higher hardness values compared to a thermoplastic PIB, which is visco-elastic at room temperature. This can be supported by TGA thermal analysis (**Figure 4.6a**), where PDMS has a higher thermal stability than PIB as the on-set decomposition temperature is much higher.

4.2.8 Summary

Currently, poly(isobutylene) (PIB) based thermoplastic polymers, known for having the lowest moisture vapor transmission rate (MVTR) among various sealant materials, is used as an edge seal to protect the PV modules from moisture ingress. However, due to its nature of the vulnerability to UV exposure, a plethora of carbon-black fillers is incorporated as UV absorbers and blockers, which in turn deprives the PIB polymer of its transparency. In this study, we have developed a PDMS-PIB mixture for PV module encapsulants. Noticeable results indicated that adding 33% of PIB into the PDMS mixture increases the moisture stability, maintains the thermal stability, and showing the least amount of hardness lost among the PDMS-PIB blends. Also, the formulated transparent adhesives do not require an edge sealant such as the conventional non-transparent PIB with a high filler content. However, it is important to understand when even lower PIB content could even achieve better moisture blocking property and have better UV stability as PDMS content would increase. This future work should focus more on the UV stability of the formulated adhesives using the accelerating test under the UV lamp and observe their UV-degradation profiles. Also note that PDMS-PIB blends are often blended using a small amount of compatibilizer; however, this process is not suggested as the material cost for the compatibilizer is extremely high. Thus, one should conduct an experiment that can profile the effect of PIB concentration on the viscosity of the blend.

4.3 List of Publications

- **J. Hah**, M. Sulkis, K. Kim, M. Kang, K. S. Moon, S. Graham, and C. P. Wong. "Surface Modification on the Flexible Polymer Backsheets using Coupling Agents and Si_3N_4 PECVD for Roll-to-Roll Processed Solar Photovoltaic (PV) Module Packaging Application." Manuscript in Preparation.
- **J. Hah**, M. Sulkis, K. S. Moon, S. Graham, and C. P. Wong. "UV Degradation of Thermally-Cured EVA Encapsulant," Manuscript in Preparation.
- **J. Hah**, Y. Kim, P. Fernandez-Zelaia, S. Hwang, S. Lee, L. Christie, P. Houston, S. Melkote, K. S. Moon, and C. P. Wong. "Comprehensive Comparative Analysis of Microstructure of Sn-Ag-Cu (SAC) Solder Joints by Traditional Reflow and Thermo-Compression Bonding (TCB) Processes," *Materialia*, 2019. Accepted.
- Y. Kim, **J. Hah**, K. S. Moon, and C. P Wong. "Novel Decapsulation Method for Silver-based Wire Bond Semiconductor Packages with High Reliability using Mixed Salt Acid Chemistry," *IEEE Transactions on Components, Packaging and Manufacturing Technology (CPMT)*, 2019. In Review.
- J. Li, B. Song, K. S. Moon, **J. Hah**, X. Wang, R. Zhang, and C. P. Wong. "High Temperature Treatment for Preparing Polysulfide Sealant/Ag Composite with High Electrical Conductivity and its Mechanism," *Composites Science and Technology, Part B: Engineering*, 2019. In Review.
- F. Wu, B. Song, **J. Hah**, C. C. Tuan, K. S. Moon, and C. P. Wong. "Polyimide incorporated cyanate ester/epoxy copolymers for high-temperature molding compounds," *Journal of Polymer Science Part A: Polymer Chemistry*, vol. 56, no.21, pp. 2412-2421, 2018.

- B. Song, J. Li, F. Wu, S. Patel, **J. Hah**, X. Wang, K. S. Moon, and C. P. Wong. "Processing and characterization of silver-filled conductive polysulfide sealants for aerospace applications," *Soft Matter*, vol. 14, no. 44, 9036-9043, 2018.
- **J. Hah**, M. Sulkis, C. Ren, M. Kang, K. S. Moon, S. Graham, and C. P. Wong. "Moisture Barrier, Mechanical, and Thermal Properties of PDMS-PIB Blends for Solar Photovoltaic (PV) Module Encapsulant," in *2019 IEEE 69th Electronic Components and Technology Conference (ECTC)*, 2019. In Press.
- **J. Hah**, Y. Kim, P. Fernandez-Zelaia, S. Lee, L. Christie, P. Houston, S. Melkote, K. S. Moon, and C. P. Wong. "Microstructure of Pb-Free Solder Joints by Reflow and Thermo-Compression Bonding (TCB) Process," in *2019 IEEE 69th Electronic Components and Technology Conference (ECTC)*, 2019. In Press.
- Y. Kim, **J. Hah**, K. S. Moon, and C. P. Wong. "Reduction of Ag Corrosion Rate during Decapsulation of Ag Wire Bond Packages," in *2019 IEEE 69th Electronic Components and Technology Conference (ECTC)*, 2019. In Press.
- **J. Hah**, B. Song, K. S. Moon, S. Graham, and C. P. Wong. "Design and Surface Modification of PET Substrates Using UV/Ozone Treatment for Roll-to-Roll Processed Solar Photovoltaic (PV) Module Packaging," in *2018 IEEE 68th Electronic Components and Technology Conference (ECTC)*, 2018, pp. 2397-2403.

REFERENCES

[1] V. Sharma and S. S. Chandel, "Performance and degradation analysis for long term reliability of solar photovoltaic systems: A review," *Renewable and Sustainable Energy Reviews,* vol. 27, pp. 753-767, 2013.

[2] M. C. C. d. Oliveira, A. S. A. Diniz Cardoso, M. M. Viana, and V. d. F. C. Lins, "The causes and effects of degradation of encapsulant ethylene vinyl acetate copolymer (EVA) in crystalline silicon photovoltaic modules: A review," *Renewable and Sustainable Energy Reviews,* vol. 81, pp. 2299-2317, 2018/01/01/ 2018.

[3] M. S. Dresselhaus and I. L. Thomas, "Alternative energy technologies," *Nature,* vol. 414, pp. 332-337, 2001.

[4] C. P. Wong, "Recent Advances in IC Passivation and Encapsulation: Process Techniques and Materials," in *Polymers for Electronic & Photonic Applications,* C. P. Wong, Ed. AT&T Bell Laboratories: Elsevier Science & Technology Books, 1992, pp. 169-172.

[5] H. S. Ullal, "Overview and Challenges of Thin Film Solar Electric Technologies," in *World Renewable Energy Congress X and Exhibition 2008*, Glasgow, Scotland, United Kingdom, 2008.

[6] "DuPont Photovoltaic Solutions," DuPont, Ed., ed, 2015.

[7] D. L. King, M. A. Quintana, J. A. Kratochvil, D. E. Ellibee, and B. R. Hansen, "Photovoltaic module performance and durability following long-term field exposure," *Progress in Photovoltaics: Research and Applications,* vol. 8, no. 2, pp. 241-256, 2000.

[8] A. W. Czanderna and F. J. Pern, "Encapsulation of PV modules using ethylene vinyl acetate copolymer as a pottant: A critical review," *Solar Energy Materials and Solar Cells,* vol. 43, no. 2, pp. 101-181, 1996.

[9] W. H. Holley, S. C. Agro, J. P. Galica, and R. S. Yorgensen, "UV stability and module testing of nonbrowning experimental PV encapsulants," in *Conference Record of the Twenty Fifth IEEE Photovoltaic Specialists Conference - 1996*, Washington, DC, USA, 1996, pp. 1259-1262.

[10] F. J. Pern and S. H. Glick, "Improved photostability of NREL-developed EVA pottant formulations for PV module encapsulation," in *Conference Record of the Twenty Sixth IEEE Photovoltaic Specialists Conference - 1997*, Anaheim, CA, USA, 1997, pp. 1089-1092.

[11] M. A. Green *et al.*, "Solar cell efficiency tables (Version 53)," *Progress in Photovoltaics: Research and Applications,* vol. 27, no. 1, pp. 3-12, 2019.

[12] Y. Y. a. J. You, "Make perovskite solar cells stable," in *Nature* vol. 544, ed: Springer Nature, 2017, pp. 155-156.

[13] B. Li, Y. Li, C. Zheng, D. Gao, and W. Huang, "Advancements in the stability of perovskite solar cells: degradation mechanisms and improvement approaches," *RSC Advances,* 10.1039/C5RA27424A vol. 6, no. 44, pp. 38079-38091, 2016.

[14] Z. Wang, Z. Shi, T. Li, Y. Chen, and W. Huang, "Stability of Perovskite Solar Cells: A Prospective on the Substitution of the A Cation and X Anion," *Angewandte Chemie International Edition,* vol. 56, no. 5, pp. 1190-1212, 2017.

[15] T. A. Berhe *et al.*, "Organometal halide perovskite solar cells: degradation and stability," *Energy & Environmental Science,* 10.1039/C5EE02733K vol. 9, no. 2, pp. 323-356, 2016.

[16] R. Cheacharoen *et al.*, "Encapsulating perovskite solar cells to withstand damp heat and thermal cycling," *Sustainable Energy & Fuels,* 10.1039/C8SE00250A vol. 2, no. 11, pp. 2398-2406, 2018.

[17] L. Shi *et al.*, "Accelerated Lifetime Testing of Organic–Inorganic Perovskite Solar Cells Encapsulated by Polyisobutylene," *ACS Applied Materials & Interfaces,* vol. 9, no. 30, pp. 25073-25081, 2017.

[18] S. Kirsten, M. Schubert, M. Braunschweig, G. Woldt, T. Voitsekhivska, and K. Wolter, "Biocompatible packaging for implantable miniaturized pressure sensor device used for stent grafts: Concept and choice of materials," in *2014 IEEE 16th Electronics Packaging Technology Conference (EPTC)*, 2014, pp. 719-724.

[19] M. D. Kempe, D. Panchagade, M. O. Reese, and A. A. Dameron, "Modeling moisture ingress through polyisobutylene-based edge-seals," *Progress in Photovoltaics: Research and Applications,* vol. 23, no. 5, pp. 570-581, 2015.

[20] K. Hwang *et al.*, "Toward Large Scale Roll-to-Roll Production of Fully Printed Perovskite Solar Cells," *Advanced Materials,* vol. 27, no. 7, pp. 1241-1247, 2015.

[21] H. C. Weerasinghe, Y. Dkhissi, A. D. Scully, R. A. Caruso, and Y.-B. Cheng, "Encapsulation for improving the lifetime of flexible perovskite solar cells," *Nano Energy,* vol. 18, pp. 118-125, 2015.

[22] D. Vak *et al.*, "3D Printer Based Slot-Die Coater as a Lab-to-Fab Translation Tool for Solution-Processed Solar Cells," *Advanced Energy Materials,* vol. 5, no. 4, p. 1401539, 2015.

[23] T. Leijtens, K. Bush, R. Cheacharoen, R. Beal, A. Bowring, and M. D. McGehee, "Towards enabling stable lead halide perovskite solar cells; interplay between structural, environmental, and thermal stability," *Journal of Materials Chemistry A,* 10.1039/C7TA00434F vol. 5, no. 23, pp. 11483-11500, 2017.

[24] R. Cheacharoen, N. Rolston, D. Harwood, K. A. Bush, R. H. Dauskardt, and M. D. McGehee, "Design and understanding of encapsulated perovskite solar cells to withstand temperature cycling," *Energy & Environmental Science*, 10.1039/C7EE02564E vol. 11, no. 1, pp. 144-150, 2018.

[25] S. M. d. L. Coelho, "Selection of Paste and Glue Elements for CPV Modules," Department of Geographical Engineering, Geophysics and Energy, University of Lisbon, 2010.

[26] M. Kempe, "Overview of Scientific Issues Involved in Selection of Polymers for PV Applications," presented at the IEEE Photovoltaic Specialists Conference (PVSC 37), Seattle, Washington, 2011.

[27] D. C. Miller, M. D. Kempe, S. H. Glick, and S. R. Kurtz, "Creep in photovoltaic modules: Examining the stability of polymeric materials and components," in *2010 35th IEEE Photovoltaic Specialists Conference*, 2010, pp. 000262-000268.

[28] M. D. Kempe, G. J. Jorgensen, K. M. Terwilliger, T. J. McMahon, C. E. Kennedy, and T. T. Borek, "Acetic acid production and glass transition concerns with ethylene-vinyl acetate used in photovoltaic devices," *Solar Energy Materials and Solar Cells*, vol. 91, no. 4, pp. 315-329, 2007.

[29] P. Hacke *et al.*, "System voltage potential-induced degradation mechanisms in PV modules and methods for test," in *2011 37th IEEE Photovoltaic Specialists Conference*, 2011, pp. 000814-000820.

[30] G. T. a. J. Kuitche, "Accelerated Lifetime Testing of Photovoltaic Modules," Photovoltaic Reliability Laboratory, Arizona State University, Solar America Board for Codes and Standards2013.

[31] F. J. Pern and G. J. Jorgensen, "Enhanced Adhesion of EVA Laminates to Primed Glass Substrates Subjected to Damp Heat Exposure," in *The 31st IEEE Photovoltaics Specialists Conference and Exhibition*, Lake Buena Vista, Florida, 2005: NREL.

[32] K. Gotoh, A. Yasukawa, and Y. Kobayashi, "Wettability characteristics of PET films treated by atmospheric pressure plasma and ultraviolet excimer light," *Polymer Journal*, vol. 43, pp. 545-551, 2011.

[33] G. J. Jorgensen *et al.*, "Moisture transport, adhesion, and corrosion protection of PV module packaging materials," *Solar Energy Materials and Solar Cells*, vol. 90, no. 16, pp. 2739-2775, 2006.

[34] M. J. Walzak *et al.*, "UV and ozone treatment of polypropylene and poly(ethylene terephthalate)," *Journal of Adhesion Science and Technology*, vol. 9, no. 9, pp. 1229-1248, 1995.

[35] J. Hah, B. Song, K. Moon, S. Graham, and C. P. Wong, "Design and Surface Modification of PET Substrates Using UV/Ozone Treatment for Roll-to-Roll Processed Solar Photovoltaic (PV) Module Packaging," in *2018 IEEE 68th Electronic Components and Technology Conference (ECTC)*, 2018, pp. 2397-2403.

[36] Z. Z. You and J. Y. Dong, "Oxygen plasma treatment effects of indium-tin oxide in organic light-emitting devices," *Vacuum*, vol. 81, no. 7, pp. 819-825, 2007.

[37] K.-X. Ma, C.-H. Ho, F. Zhu, and T.-S. Chung, "Investigation of surface energy for organic light emitting polymers and indium tin oxide," *Thin Solid Films*, vol. 371, no. 1, pp. 140-147, 2000.

[38] J. S. Kim, R. H. Friend, and F. Cacialli, "Surface energy and polarity of treated indium–tin–oxide anodes for polymer light-emitting diodes studied by contact-angle measurements," *Journal of Applied Physics*, vol. 86, no. 5, pp. 2774-2778, 1999.

[39] J. S. Kim, R. H. Friend, and F. Cacialli, "Surface wetting properties of treated indium tin oxide anodes for polymer light-emitting diodes," *Synthetic Metals*, vol. 111-112, pp. 369-372, 2000.

[40] G. Ström, M. Fredriksson, and P. Stenius, "Contact angles, work of adhesion, and interfacial tensions at a dissolving Hydrocarbon surface," *Journal of Colloid and Interface Science*, vol. 119, no. 2, pp. 352-361, 1987.

[41] N. Verplanck, Y. Coffinier, V. Thomy, and R. Boukherroub, "Wettability Switching Techniques on Superhydrophobic Surfaces," *Nanoscale Research Letters*, vol. 2, no. 12, p. 577, 2007.

[42] C. Dorrer and J. Rühe, "Drops on Microstructured Surfaces Coated with Hydrophilic Polymers: Wenzel's Model and Beyond," *Langmuir*, vol. 24, no. 5, pp. 1959-1964, 2008.

[43] J.-H. Oh, T.-J. Ko, M.-W. Moon, and C. H. Park, "Nanostructured fabric with robust superhydrophobicity induced by a thermal hydrophobic ageing process," *RSC Advances*, 10.1039/C7RA03801A vol. 7, no. 41, pp. 25597-25604, 2017.

[44] N. Majoul, S. Aouida, and B. Bessaïs, "Progress of porous silicon APTES-functionalization by FTIR investigations," *Applied Surface Science*, vol. 331, pp. 388-391, 2015.

[45] C. L. Loch, D. Ahn, C. Chen, J. Wang, and Z. Chen, "Sum Frequency Generation Studies at Poly(ethylene terephthalate)/Silane Interfaces: Hydrogen Bond Formation and Molecular Conformation Determination," *Langmuir*, vol. 20, no. 13, pp. 5467-5473, 2004.

[46] C.-H. Chiang, H. Ishida, and J. L. Koenig, "The structure of γ-aminopropyltriethoxysilane on glass surfaces," *Journal of Colloid and Interface Science,* vol. 74, no. 2, pp. 396-404, 1980.

[47] W. K. T. Kobayashi, M. Arisawa, and K. L. Mittal, K. L. Mittal, Ed. *Polymer Surface Modification: Relevance to Adhesion*. 2009.

[48] M. J. Shenton and G. C. Stevens, "Surface modification of polymer surfaces: atmospheric plasma versus vacuum plasma treatments," *Journal of Physics D: Applied Physics,* vol. 34, no. 18, p. 2761, 2001.

[49] Z. Zhu and M. J. Kelley, "IR spectroscopic investigation of the effect of deep UV irradiation on PET films," *Polymer,* vol. 46, no. 20, pp. 8883-8891, 2005.

[50] T. N. Murakami, Y. Fukushima, Y. Hirano, Y. Tokuoka, M. Takahashi, and N. Kawashima, "Modification of PS films by combined treatment of ozone aeration and UV irradiation in aqueous ammonia solution for the introduction of amine and amide groups on their surface," *Applied Surface Science,* vol. 249, no. 1, pp. 425-432, 2005.

[51] F. M. Fowkes, "Role of acid-base interfacial bonding in adhesion," *Journal of Adhesion Science and Technology,* vol. 1, no. 1, pp. 7-27, 1987.

[52] D. K. Owens and R. C. Wendt, "Estimation of the surface free energy of polymers," *Journal of Applied Polymer Science,* vol. 13, no. 8, pp. 1741-1747, 1969.

[53] P. Molitor, V. Barron, and T. Young, "Surface treatment of titanium for adhesive bonding to polymer composites: a review," *International Journal of Adhesion and Adhesives,* vol. 21, no. 2, pp. 129-136, 2001.

[54] C. Cai, D. C. Miller, I. A. Tappan, and R. H. Dauskardt, "Degradation of thermally-cured silicone encapsulant under terrestrial UV," *Solar Energy Materials and Solar Cells,* vol. 157, pp. 346-353, 2016.

[55] K. T. G. Jorgensen, S. Glick, J. Pern, and T. McMahon, "Materials Testing for PV Module Encapsulation," presented at the National Center for Photovoltaics and Solar Program Review Meeting, Denver, Colorado, 2003.

[56] M. C. Sulkis, "Characterization of Encapsulant and Edge Seal Materials for Flexible Solar Cell Packaging," Master of Science, The George W. Woodruff School of Mechanical Engineering Georgia Institute of Technology, 2019.

[57] E. Plueddemann, "Silane Coupling Agents," in *Nature of Adhesion through Silane Coupling Agents*2 ed. New York, NY: Springer, 1991, pp. 111-139.

[58] P. P. a. E. Plueddeman., "History of Polymeric Composites," in *History of silane coupling agents in polymer composites*, vol. 14 ed. Utrecht, The Netherlands: VSP, 1986, pp. 105-139.

[59] N. Z. C. Girardeaux, M. Art, B. Gillion, J. J. Pireaux, and R. Caudano, "Animation of Poly(Ethylene-Terephthalate) Polymer Surface for Biochemical Applications," *Plasmas and Polymers,* vol. 1, no. 4, 1996.

[60] A. Vesel and M. Mozetic, "Modification of PET surface by nitrogen plasma treatment," *Journal of Physics: Conference Series,* vol. 100, no. 1, 2008.

[61] Y. Deslandes, G. Pleizier, E. Poiré, S. Sapieha, M. R. Wertheimer, and E. Sacher, "The Surface Modification of Pure Cellulose Paper Induced by Low-Pressure Nitrogen Plasma Treatment," *Plasmas and Polymers,* vol. 3, no. 2, pp. 61-76, 1998.

[62] D. J. Wilson, R. L. Williams, and R. C. Pond, "Plasma modification of PTFE surfaces. Part II: Plasma-treated surfaces following storage in air or PBS," *Surface and Interface Analysis,* vol. 31, no. 5, pp. 397-408, 2001.

[63] M.-J. Wang, Y.-I. Chang, and F. Poncin-Epaillard, "Acid and basic functionalities of nitrogen and carbon dioxide plasma-treated polystyrene," *Surface and Interface Analysis,* vol. 37, no. 3, pp. 348-355, 2005.

[64] J. M. Grace and L. J. Gerenser, "Plasma Treatment of Polymers," *Journal of Dispersion Science and Technology,* vol. 24, no. 3-4, pp. 305-341, 2003.

[65] E. Uchida, Y. Uyama, and Y. Ikada, "Surface graft polymerization of acrylamide onto poly(ethylene terephthalate) film by UV irradiation," *Journal of Polymer Science Part A: Polymer Chemistry,* vol. 27, no. 2, pp. 527-537, 1989.

[66] C. Decker and A. D. Jenkins, "Kinetic approach of oxygen inhibition in ultraviolet- and laser-induced polymerizations," *Macromolecules,* vol. 18, no. 6, pp. 1241-1244, 1985.

[67] J. Gardella, S. A. Ferguson, and R. L. Chin, "$\pi^* \leftarrow \pi$ Shakeup Satellites for the Analysis of Structure and Bonding in Aromatic Polymers by X-Ray Photoelectron Spectroscopy," vol. 40, no. 2, pp. 224-232, 1986.

[68] S. F. Fairgrieve, *Degradation and Stabilisation of Aromatic Polyesters*. ISmithers, 2009.

[69] M. Rubino, S. Netramai, R. Auras, and B. A. Annous, "Effect of chlorine dioxide gas on physical, thermal, mechanical, and barrier properties of polymeric packaging materials," *Journal of Applied Polymer Science,* vol. 115, no. 3, pp. 1742-1750, 2010.

[70] X. X. J. W. He, J. S. Corneille, and D. W. Goodman, "X-ray photoelectron spectroscopic characterization of ultra-thin silicon oxide films on a Mo(100) surface," *Surface Science,* vol. 279, pp. 119-126, 1992.

[71] X. Peng, Y. Huang, T. Xia, M. Kong, and G. Li, "Shapes of dispersed phase in confined PIB/PDMS blends with different compositions during shear flow," *European Polymer Journal,* vol. 47, no. 10, pp. 1956-1963, 2011.

[72] J. A. d. Cueto and T. J. McMahon, "Analysis of leakage currents in photovoltaic modules under high-voltage bias in the field," *Progress in Photovoltaics: Research and Applications,* vol. 10, no. 1, pp. 15-28, 2002.

[73] V. Šály, M. Ružinský, and P. Redi, "Chapter 437 - Testing of Photovoltaic Modules and Encapsulations at Elevated Voltage, Temperature and Humidity," in *World Renewable Energy Congress VI*, A. A. M. Sayigh, Ed. Oxford: Pergamon, 2000, pp. 2053-2056.

[74] K. R. McIntosh, N. E. Powell, A. W. Norris, J. N. Cotsell, and B. M. Ketola, "The effect of damp-heat and UV aging tests on the optical properties of silicone and EVA encapsulants," *Progress in Photovoltaics: Research and Applications,* vol. 19, no. 3, pp. 294-300, 2011.